Monte Carlo for Preclinical Radiotherapy

A THESIS PRESENTED
BY
Rajit Tummala
TO THE
Biological Sciences Collegiate Division

IN PARTIAL FULFILLMENT OF THE REQUIREMENTS
FOR THE DEGREE OF
Bachelor of Science
IN THE SUBJECTS OF
Biological Sciences and Mathematics

The College, University of Chicago
Chicago, Illinois
May 2024

Thesis Advisor: Bulent Aydogan, PhD Rajit Tummala

Monte Carlo for Preclinical Radiotherapy

Abstract

Radiotherapy is a cancer treatment that uses high-energy X-rays to kill cancer cells. A major challenge in treating cancer is the heterogeneity of the disease. Preclinical models are important translational tools to study this heterogeneity's impact on treatment efficacy, but there have been many challenges in scaling preclinical radiotherapy due to the scale of small animals and lower orthovoltage energy range (100-500 kV) used for treatments. One major challenge is accurate dose calculations. Monte Carlo (MC) methods, a repeated random sampling technique, is a promising approach. Two computational approaches employing these MC methods, high-performance computing (HPC-MC) and graphics processing unit computing (GPU-MC), are studied for their applications in preclinical radiotherapy. HPC-MC, running a full MC approach, will be a vital validation tool for faster dose calculation algorithms, especially in higher order treatment planning and inverse planning. GPU-MC, running a fast MC approach, will be an important tool for treatment planning software and inverse planning optimization. Ultimately, HPU-MC and GPU-MC will help usher a much-needed paradigm shift in preclinical radiotherapy from dose to a patient to dose distributions within a patient.

Contents

Figures

Tables

Dedicated to my family.

Acknowledgments

There are many people I would like to thank, and whom without, this thesis would not have been possible.

After my first year in college, I was matched for a summer research project with Jordan Slagowski. It is thanks to him that I am writing this thesis. He introduced me to the small animal radiotherapy project that motivates this work. Through him, I met Erik Pearson and Bulent Aydogan, who welcomed me into their lab with open arms. The high-performance computing Monte Carlo model that is the focus of this thesis comes from Erik's original work. Jordan, Erik, and Bulent spent countless hours over these three years helping me plan experiments, figure out the next steps, submit our work for conferences, and secure funding. They always strove to put me in the best position to succeed and were selfless with their time. I cannot express how grateful I am for their mentorship, kindness, and friendship over these three years.

I would also like to thank my thesis readers, Patrick La Riviere and Howard Halpern, for their revisions and support of this work. Patrick is the director of the BSCD SURFBOARD research fellowship, which funded my research for two summers after my first and second year. His weekly check-ins were something I always looked forward to. He always went out of his way to make sure we had everything we needed and that we felt supported. Howard is the director of the Center for EPR Imaging In Vivo Physiology. All the mouse data and preclinical radiotherapy experimental data that is in this thesis is thanks to the efforts of his lab.

Finally, I would like to thank my friends and family for their support. My friends and family made the lows of college tolerable and the highs of college that much sweeter.

To my mother and father, who have made many sacrifices in their life for the future of mine, I love you. When I think about the person I hope to be, I think of both of you.

1

Introduction

1.1 Background and Significance

Cancer is and will be a major health problem. Currently, there are over 9 million deaths worldwide from cancer each year [1]. Over the next two decades, the number of people expected to be diagnosed with cancer will nearly double from 18.1 million to 29.5 million [2].

In the US, one in three Americans will be diagnosed with an invasive cancer in their lifetime [3]. Although the incidence of cancer seems to paint a bleak image, that is far from the truth. In fact, the death rate from cancer has dropped by one-third since 1991—over 3 million lives saved largely due to advances in cancer treatments [4].

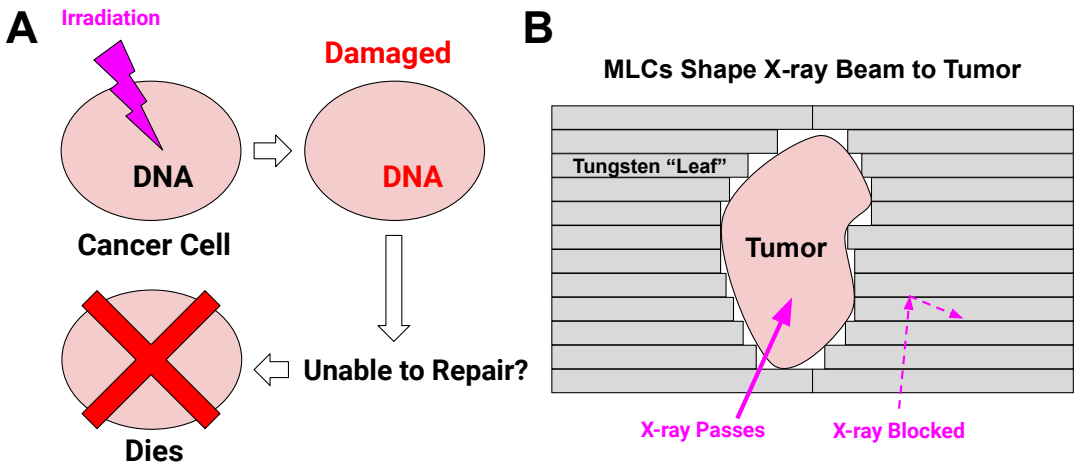

Figure 1.1: Radiotherapy Basics. A) illustrates how irradiation induces breaks in DNA within cells, and if these breaks are not repaired, the cell dies, B) depicts multi-leaf collimators (MLCs) used in clinical radiotherapy to shape the radiation beam to the tumor and minimize damage to surrounding healthy tissue.

Radiotherapy is one such treatment that uses high-energy X-rays to kill cancer cells. The main challenge of radiotherapy is precisely delivering these X-rays to cancerous tissue without damaging the surrounding healthy tissue. Advances in imaging, treatment planning, and delivery precision have addressed this challenge. Currently, radiotherapy can cure many early-stage and locally-advanced tumors with minimal adverse side effects. For late-stage cases, palliative radiotherapy can ease cancer-related symptoms [5]. Radiotherapy can treat cancer in a variety of places in the body from brain tumors to colorectal cancers. Physicians can also combine radiotherapy with other cancer therapies to improve treatment odds and minimize

treatment risk [6]. In short, radiotherapy is and will be an indispensable tool to treat cancer.

A major challenge in treating cancer is the heterogeneity of the disease. Similarly presenting cancers can have different genetic profiles, physiologies, and microenvironments that vary patient-to-patient and determine the success of a treatment [7]. For instance, hypoxia (low oxygen concentration) in tumors has been shown to reduce the effectiveness of radiotherapy, chemotherapy, and immunotherapy [8]. Advances in functional imaging, genetic profiling, and biological categorization of tumors will only continue to provide clinicians with more and more information about a patient's cancer. As a consequence, the next frontier in oncology—called precision oncology—is cancer treatment tailored to the patient. How can we best treat a patient given the characteristics of their cancer? This fundamental question can be divided into two interconnected aims: (1) optimize radiotherapy to the patient's tumor biology and (2) optimize the patient's tumor biology for radiotherapy.

To elucidate these two aims, researchers turn to preclinical models such as mice. In these models, they can provide evidence of a therapy's potential for clinical trials and better test research hypotheses. The ability to scale up preclinical research to humans is dependent on how well the preclinical model and treatment mimics the clinical protocols and realities. One of the main challenges of research in radiotherapy is this lack of an analogous preclinical system. When scaling down radiotherapy from humans to mice, researchers run into many problems. For planning treatments, dose calculations in mice are more challenging due to the lower energy range, which requires more information for accurate predictions [9]. For delivering treatments, clinical systems use multi-leaf collimators (MLCs), consisting of many highly attenuating (typically tungsten) leaves, to shape radiation beams to avoid damage to healthy tissue as shown in panel B of Figure 1.1. However, humans are roughly 3,000-fold

larger than mice (and roughly 14-fold in a linear dimension), so scaling down these MLCs for small animals has been challenging [10, 11].

In the following work, we will address the challenges of preclinical treatment planning and delivery. Then, we will discuss the use of Monte Carlo methods, a repeated random sampling technique, to perform more accurate dose calculations at the orthovoltage scale (100-500 kV). We will explore two computational approaches employing these Monte Carlo methods, high-performance computing (HPC-based) and graphics processing unit computing (GPU-based), for their potential applications in preclinical radiotherapy. We will conclude with a summary of the work's findings and future directions.

1.2 Preclinical Radiotherapy

Preclinical radiotherapy typically involves the treatment of small animals like mice to test and validate a new experimental treatments prior to running clinical trials. Often, this explores how to integrate the increasing amount of imaging data about the tumor and its environment into optimizing radiotherapy plans. For instance, tumors can be characterized as hypoxic when oxygen levels are not sufficient for proper maintenance of cellular processes [12]. For over century, hypoxic tissue is known to be more resistant to radiotherapy [13]. When a subregion of a tumor tissue is hypoxic, this resistance can cause eventual treatment failure in patients receiving radiotherapy. An important question is evaluating the benefit of a locally increased (aka boost) dose to the hypoxic part of the tumor. Testing this question in the patients is difficult because a boost dose could come with an increased collateral dose to healthy tissues, which leads to a greater risk of side effects. Preclinical models enable the

risk-to-reward of experimental treatments to be evaluated before clinical implementation. For instance, recent boost dose to the hypoxic region has shown promise for three cancer types in mice [14]. But the results have been mixed in clinical trials, suggesting there might be particular use cases. Further, there several unknown variables for this form of adaptive radiotherapy, such as the magnitude of the boost dose for effective and safe outcomes, potential demographic or genetic contraindications, and the optimal method of synergizing this treatment with other cancer treatments [15].

In addition to tailoring radiotherapy to the tumor biology, the converse approach is equally important—specifically how tumor biology can be altered to improve radiotherapy outcomes. For instance, polymerase theta (POLΘ) is an enzyme involved in DNA repair overexpressed in cancers [16]. The repair pathway of the enzyme is vital to microhomology-mediated end-joining, typically considered a backup to the two main DNA repair pathway for double-stranded breaks (non-homologous end-joining and homologous recombination) in eukaryotes [17]. A gene knockdown using small interfering RNA (siRNA) is a method to lower protein expression by targeting a protein's messenger RNA (mRNA) for degradation, which prevents ribosomal translation of the mRNA into the protein. Through siRNA-mediated knockdown screen of 200 genes coding for proteins involved in DNA repair *in vitro*, POLΘ was identified as a potential inhibitor target to cause radiosensitization independent of the presence of defects in repair pathways, especially viable due to the low expression in healthy tissue [18]. After the discovery of two novel small molecule inhibitors for POLΘ, mice implanted with colon cancer cells (HCT116) were given the inhibitor orally and then treated with a 2 Gy fractionated radiotherapy regime over two weeks (excluding weekends) for a total of 20 Gy. The xenograft model demonstrated tumor growth delay from POLΘ inhibition,

corroborating *in vitro* irradiation results [19]. Radiosensitivity of a cell varies based on the cell cycle stage, typically with the most sensitivity during the mitotic phase and least sensitivity during late S phase. So, a potential benefit with a fractionated regime is increasing the probability of irradiating cells while they are undergoing a more radiosensitive stage of the cell cycle [20]. Further, cells were placed in anaerobic chamber to induce hypoxic conditions and then irradiated under these same conditions to test the radiosensitization capability of POLΘ for hypoxic tissue. The results demonstrate POLΘ inhibition can radiosensitize independent of cellular oxygenation *in vitro* [19]. Note normal tissue could be already radiosensitive due to their oxygenation, so the application would be for targeting stubborn radioresistant subregions of the tumor like the hypoxic region to improve the therapeutic ratio of tumor cell death to healthy cell death. The case of POLΘ illustrates the potential to exploit biological machinery to approach current hurdles in radiotherapy treatment like a hypoxia.

Ideally, preclinical radiotherapy should be analogous to clinical radiotherapy in treatment planning and execution. The further it deviates from clinical realities, the greater risk of producing results that are not translatable. Traditionally, translational research requires testing in an *in vivo* preclinical model after *in vitro* proof of concept to justify clinical trials and implementation [21]. Currently, clinical radiotherapy has evolved towards highly non-uniform and conformal dose distributions that cannot be accurately mimicked at the preclinical level. Small animal irradiation technology lags behinds clinical innovations to improve tailoring dose to patients. Many animal studies still remain quite crude, targeting the whole body or employing partial shielding [22]. This is largely due to the significant challenges when scaling down treatment planning and execution to the preclinical level [23].

1.3 Challenges in Translational Radiotherapy

1.3.1 Treatment Planning

Ideally, preclinical treatment planning software would have all the functionality of clinical treatment planning software. For instance, for more complex plans, there would be tools for inputting and visualizing the spatial arrangement of radiation beams [24]. Further, there would be tools for segmenting imaging data to delineate organs of risk from target tumor regions, registering multiple sets of imaging data to allow for multimodal planning, and analyze treatment plan quality with dose-volume histograms and dose difference plots [25]. Preclinical treatment planning systems would have to handle the small voxels from preclinical multimodal imaging. For instance, voxel resolution of CBCT can be around 100 microns [9]. Additionally, clinical radiotherapy is performed over course of multiple sessions, called treatment fractions, to improve sparing of healthy tissue; normal tissue has more robust repair mechanisms than cancerous tissue, and due to this, healthy tissue repairs itself better in that time. The accumulation over many fractions improves the differential between the probability of healthy tissue and tumor tissue damage, also known as therapeutic ratio [26]. Although typical small animal radiotherapy experiments administer dose in single session to an anesthetized animal, some biological studies would benefit from the capability to fractionate treatment delivery, which would require tools such as deformable image registration, to align imaging sets across treatment sessions to measure the total dose accumulation [25]. A preclinical treatment system should offer comparable tools for the planning and execution of fractionated radiotherapy experiments.

The two main vendors of small animal irradiators have provided these tools: SmART-Plan from Precision X-Ray Inc. (Madison, CT, USA) and Muriplan from Xstrahl Ltd. (Surrey, UK). Both software perform dose calculation using GPU-based Monte Carlo or superposition/convolution algorithm [27]. Third-party treatment planning software such as μ-RayStation and SmART-XPS has been recently developed for these preclinical irradiators as well. A main limitation of most software currently is the ability for only forward planning, or in other words, the inability to create a plan based on the optimization of an objective function that weights different treatment goals. This technique, called inverse planning, is a critical step in intensity-modulated radiotherapy [28]. Traditionally, most clinical treatment systems use analytical or convolution/superposition algorithms for inverse planning [29]. These algorithms do not scale well typically for kilovoltage beams used in preclinicial radiotherapy due to way dose is computed. For instance, convolution/superposition can underestimate dose up to 300% in high atomic number regions which the algorithm traditionally cannot account for, although steps have been made to adapt it for these circumstances [30, 31]. For the inverse planning to design 3D-printed compensators for small animal radiotherapy, a modified open-source pencil beam algorithm was used but dose calculations rely only upon electron density for its calculations, so dose calculation accuracy in heterogeneous regions, particularly those with high atomic numbers, is still a concern at the kilovoltage scale [11]. A fast Monte Carlo algorithm, which leverages variance reduction techniques and optimized cutoff parameters in transport, could be promising for inverse planning due its accuracy in heterogeneities for kilovoltage photons [25, 32].

Many clinical treatment planning systems often rely on bulk density overrides using tissue segmentations for dose calculations which depend on accurate segmentation and over-

shadow heterogeneous contributions to the actual dose delivered [23]. However, due to fundamental differences clinical and preclinical radiotherapy such as the energy range used, this dose calculation approach can lead much greater error in preclinical treatment planning. For dose calculations, the megavoltage energy range (commonly 6-18 MV) used for clinical treatments generally requires only the density of the material for accurate dose calculations during planning. In contrast, the lower kilovoltage energy range used for preclinical treatments requires atomic composition of the material in addition to density for accurate dose calculations for comparable levels of accuracy [9]. Part of the challenge is not only the scale of small animals, but also the fact that ionizing photon radiation interactions change in probability of occurrence based on the energy of the photon. This is also known as the energy-dependence of cross sections for interaction types. For instance, the requirement for atomic composition occurs due to an increased cross section of the photoelectric effect for kV photons relative to Compton scatter. For MV photons, the photoelectric effect is more negligible in occurrence relative to Compton scatter.

There are four main ionizing interactions of photons with atoms: coherent scattering (Rayleigh and Thomson scattering), photoelectric absorption, Compton scattering, and pair production. Coherent scattering is often negligible relative to other photon interactions and pair production only becomes dominant after 25 MeV (Mega Electron Volt) [33]. Compton scattering increases in probability with greater photon energy up to a certain point and then decreases, but is mostly independent of the material's atomic number (Compton Scatter Probability $\propto \frac{1}{E}$ after 0.1 MeV). It is the most prominent interaction in typical clinical radiotherapy MeV radiotherapy ranges (6-18 MeV). In contrast, the photoelectric effect is largely dependent on atomic number and energy, mainly decreasing as photon energy increases ex-

cluding the resonance peak (Photoelectric Probability $\propto \frac{Z^3}{E^3}$). Although Compton scatter becomes dominant (or more probable) around 0.1-0.15 MeV, the photoelectric effect does not become negligible in the preclinical energy range (typically at most 0.225 MeV with a 225 kVp X-ray tube) [34]. Furthermore, the cubic dependence on atomic number further compounds the photoelectric effect's salience at the kilovoltage scale in higher atomic number materials.

A challenge then becomes to how to extract this extra information required for accurate preclinical dose calculations. One method has been to deduce and assign the atomic composition to voxels based on the acquired imaging data. Further, one could segment the imaging data and then assign a specific material to each of these segmentation rather than based on voxel values. However, evidence suggests dose measurements could deviate up to 40% due to misaligned tissue segmentation at the kilovoltage energy range, whereas these same segmentation errors deviate less than 10% at the megavoltage energy range [23, 35]. Another approach would be to convert values of the imaging data into material property assignments through a function fitting empirical data. The approach has been adapted for the cone beam computed tomography (CBCT) used in preclinical radiotherapy to decrease the dose error to around 4%, which improves upon bulk overrides of segmentations but still does not meet the clinical threshold of 2% error [36]. Altogether, some current limitations in preclinical treatment planning are the absence of inverse planning tools, limited accuracy of dose calculation algorithms due to a trickier lower energy range, and the best way to extract material assignments needed for accurate dose calculations from imaging data.

1.3.2 Plan Delivery

For treatment execution, preclinical radiotherapy studies often use collimators ranging from 1 mm to several centimeters. Smaller field sizes, especially field sizes smaller than the focal spot of the X-ray tube (diameter of 3 mm for the larger focal spot used during treatment), can cause the output of the irradiator to drop due to an obscuring and non-uniform spatial distribution of the electron focal spot on the anode target. Further, these lower field sizes lose the presence of scatter equilibrium in tissue. [32, 37]. Additionally, since the electron beam source collides into a metal anode target to produce an X-ray beam orthogonal to the beam source, there also exists a non-uniform fluence and energy distribution of X-ray emissions along the anode-cathode axis, known as the heel effect. In particular, X-ray emissions at more acute angles, closer the cathode size, possess a greater fluence (or intensity) and a lower mean radiation energy since at more obtuse angles, the anode heel absorbs low-energy photons [38]. Secondary collimation in preclinical irradiators helps correct for the heel effect [32].

For execution of more complex treatments in the clinic, such as 3D-conformal, intensity-modulated, and volumetric-modulated arc radiotherapy, beam shaping devices consisting of dynamic, highly attenuating (tungsten) blades called multileaf collimators (MLCs) are essential. These MLCs are illustrated in panel B of Figure 1.1. MLCs modulate dose, typically at a resolution that scales to 1 cm width at isocenter, by positioning each of these individual leaves to conform the radiation beam to the shape of the target region [39]. However, with current technology, the miniaturizing of these multileaf collimator systems to the preclinical scale has been difficult [40]. Some alternative approaches for dose modulation at the preclinical level

include sparse orthogonal collimators, rastered pencil beams, and 3D-printed compensators [11]. However, all of these approaches have certain problems such as long treatment times, costly engineering and implementation, poor treatment resolution, or adding additional fabrication steps.

1.4 Monte Carlo

Some challenges with modeling radiotherapy is scale of particle of interest relative to distance traveled by it, the probabilistic nature of interactions along this distance, and the number of particles that contribute to the overall macroscopic property of dose. For instance, the wavelength of an X-ray photon is about 0.01 to 10 nm. Although a photon does not have a volume in the traditional sense, treating a photon as a particle, an expression of a photon's volume can be calculated as

$$\text{photon's volume}(\lambda) \coloneqq c\lambda^3 \tag{1.1}$$

where $c = 7.394 \times 10^{-4}$ (fine structure constant divided by π^2) and λ equals the wavelength [41]. From this equation and assuming the billiard ball is an ideal sphere (with a diameter of 57 mm) and the largest X-ray photon of 10 nm, one could fit more than 2×10^{26} photons in a single billiard ball! That is more than all the human cells of every human put together on this planet currently (assuming the overestimate of 724 trillion human cells per human). To generate these X-rays, an irradiation for 60 seconds at a current of 13 mA, roughly 4.9×10^{18} electrons run across the X-ray tube. To run a full Monte Carlo simulation of 90 billion electrons using high-performance computing took about 1 week, thus to simulate the electrons across the X-ray tube for a mere 60 second irradiation would require roughly a million years!

1.4.1 Basics

Modeling any phenomenon can be divided to into two fundamental approaches: deterministic and stochastic. A deterministic model can predict a phenomenon without the introduction of a randomness. For instance, suppose one wanted to predict the area under the curve of a integrable positive function $f : \mathbb{R} \to \mathbb{R}^+$ over an interval $[a, b]$ where $a, b \in \mathbb{R}$ and $a < b$. A deterministic model F would take two inputs (a, b) and integrate from the function f over the the interval $[a, b]$ as such

$$F(a, b) \coloneqq \int_a^b f(x)\,\mathrm{d}x = \text{exact area under the curve between two points} \tag{1.2}$$

In contrast, a stochastic model predicts a phenomenon by introducing randomness. Another way to approach the same problem would be to sample a random point $r_1 \in [a, b]$. Then an estimate for the area under the curve would be

$$A_1 = f(r_1)(b - a) = \text{estimated area under the curve between two points} \tag{1.3}$$

To find an accurate estimate, one would need to sample enough random points r_i and average the areas A_i as such

$$F^N(a, b) \coloneqq \frac{1}{N}\sum_{i=1}^{N} A_i = \frac{1}{N}\sum_{i=1}^{N} f(r_i)(b - a) \tag{1.4}$$

Thus, a stochastic model F^N will approach the true value for a sufficiently large sample

$$F(a, b) = \lim_{N\to\infty} F^N(a, b) \tag{1.5}$$

For a function with a known integral in this case, a stochastic approach would take more time to approach the exact answer supplied by a deterministic model. However, when a function does not have a known integral, a stochastic approach could be quicker depending on the problem. For coupled transport problems of radiotherapy used in dose calculation, where

photons, electrons, and other particles are being transported in a user-defined space and each influence the transport of other particles, multidimensional numerical integration is required to solve the system. Here, a stochastic Monte Carlo approach can be faster. In fact, a mathematical proof can demonstrate Monte Carlo is more efficient than first-order deterministic models for transport problems with greater than four dimensions given some assumptions about the calculation and computation technique, but independent of the physics used to model the system. Typically, transport problems for radiotherapy are of dimension $6.\varepsilon$ or $7.\varepsilon$, where the first six dimensions are the position $\vec{x}$ and momentum $\vec{p}$ vectors in 3D Cartesian space, the optional seventh dimension is for time, which cannot be ignored for nonlinear problems, and the ε is the discrete dimension of particle species, charge, or intrinsic spin [42].

1.4.2 Photon Transport

The probability a photon interacts $P(x)$ over a distance x travelled in a homogeneous material is given by the attenuation law

$$P(x) \coloneqq \int_0^x \mu \mathrm{e}^{-\mu x'} \, \mathrm{d}x' \tag{1.6}$$

where μ is the linear attenuation coefficient that will depend on the medium and energy. Note if $x \to \infty$, then $P(x) \to 1$, or in other words, the probability of the photon will interact will be equal to 1. From this equation, the mean free path length λ is calculated as

$$\lambda = \int_0^\infty x \left[\mu \mathrm{e}^{-\mu x} \right] \mathrm{d}x = \frac{1}{\mu} \tag{1.7}$$

For a given distance x, it will be convenient to think of distance travelled before an interaction in terms of the number of mean free path lengths λ_n

$$\lambda_n(x) \coloneqq \frac{x}{\lambda} = x\mu \tag{1.8}$$

Then, the first equation can be integrated with the boundary condition $P(0) = 0$ and rewritten as

$$P(\lambda_n) = \int_0^{\lambda_n} \mathrm{e}^{-\lambda_n'} \, \mathrm{d}\lambda_n' = 1 - \mathrm{e}^{-\lambda_n} \tag{1.9}$$

Then, the inverse of this function can be determined such that given a uniform selection of a random number $r_1 \in [0, 1)$, the number of mean path lengths travelled by the photon in a given medium and energy will be

$$P^{-1}(r_1) = -\ln(1 - r_1) = \lambda_n \tag{1.10}$$

and thus, for a random propagation of a photon, the distance travelled till the first interaction will be

$$x(r_1) \coloneqq -\frac{1}{\mu} \ln(1 - r_1) = -\frac{1}{\mu} \ln(r_1^*) \tag{1.11}$$

Note here r_1^* is an complementary random value of r_1 where $r_1^* = 1 - r_1$ and $r_1^* \in (0, 1]$. For a photon trajectory that changes mediums N times before a point where an interaction must happen, the number of mean free path lengths travelled can be defined as

$$\lambda_n^* \coloneqq \sum_{i=0}^{N} \mu(m_i) x(m_i) \tag{1.12}$$

where $\mu(m_i)$ and $x(m_i)$ are respectively the linear attenuation coefficient and linear distance travelled in the medium during the ith change, where the zeroth is the initial medium.

Once the distance travelled till the first interaction is computed, the next step is to calculate the type of interaction experienced by the particle. For a photon, four interactions are possible: (1) coherent scattering, (2) photoelectric absorption, (3) Compton scatter, and (4) pair production. The linear attenuation coefficient can be decomposed into these constituent reactions as $\mu = \mu_1 + \mu_2 + \mu_3 + \mu_4$. Note like μ, every μ_i will be dependent on the medium and energy of the photon. Then, given a uniform random number $r_2 \in [0, 1)$, the interaction

type $i(r_2)$ will be the probability $\frac{\mu_i}{\mu}$ as such

$$i(r_2) \coloneqq \begin{cases} \text{coherent scattering} & r_2 \in \left[0, \frac{\mu_1}{\mu}\right) \\ \text{photoelectric absorption} & r_2 \in \left[\frac{\mu_1}{\mu}, \frac{\mu_1+\mu_2}{\mu}\right) \\ \text{Compton scatter} & r_2 \in \left[\frac{\mu_1+\mu_2}{\mu}, \frac{\mu_1+\mu_2+\mu_3}{\mu}\right) \\ \text{pair production} & r_2 \in \left[\frac{\mu_1+\mu_2+\mu_3}{\mu}, 1\right) \end{cases}$$

Once a interaction has been sampled, the secondary particle parameters must be determined. For instance, in the case of Compton scatter, a photon interacts with a single electron. The energy of this electron released and the angle of scatter must also then be sampled, typically through a probability distribution function of a differential cross section $\mathrm{d}\sigma/\,\mathrm{d}\Omega$ dependent on the material and photon energy. A differential cross section represents the probability that particle passing through an area $\mathrm{d}\sigma$ before scattering will pass through the solid angle $\mathrm{d}\Omega$ after scattering. For any sampled secondary particle parameters, both particles must follow kinematic conservation laws.

The steps of distance traveled till an interaction, sampling from possible interactions, and then adjusting the simulation based on the selected interaction is repeated many times to decrease noise. The central limit theorem can estimate this noise. In this case, the noise is the standard deviation of the sample distribution σ_s from the mean μ_s of this same distribution, which depends on the number of samples run N and the standard deviation of the actual distribution σ_a as $\sigma_s = \sigma_a/\sqrt{N}$. Due to the fact standard deviation decreases proportional to the square root of histories, a large number of histories is generally needed for acceptable results. Typically for a simulation to end, all these primary and secondary particles must all either fall below some threshold energy typically defined based on the particle type or exit the

space of interest. An analogous approach can also be approached for charged particles like electrons and protons [42].

1.4.3 Application

Radiotherapy dose calculation algorithms estimate the amount of energy deposited by the X-ray beam in a given volume, typically voxels of a dose grid covering structures of interest within the patient. Dose calculation algorithms can be broadly divided into three types: factor-based, model-based, and principle-based. Broadly, factor-based fit empirical measurements, model-based simplify physical processes by dividing beam fluence into kernels, and principle-based attempt to simulate all physical interactions [43]. These three algorithm types are listed in increasing order of typical calculation accuracy and computational cost. Monte Carlo employs randomness to determine the interactions experienced by a particle along a given trajectory as shown in Subsection 1.4.2, so it falls under the principle-based category. Moreover, Monte Carlo dose calculation algorithms are considered the gold standard for radiotherapy simulations because of its attempt to model all possible interactions [44].

The accuracy of a dose calculation algorithm is inherently tied to how well it models the transport and interaction of photons, which increases in complexity and importance in heterogeneous realities of radiotherapy. For commissioning of these algorithms to irradiation systems, dose profiles are measured in homogeneous water phantoms, which represent ideal circumstances. In reality, the patient's tissue can vary largely in density and atomic composition (e.g. cortical bone versus adipose tissue). Since patient tissue is heterogeneous, algorithms should account for variations. Tissue density corrections can be classified as local

energy deposition or non-local energy deposition depending on whether they account for electron transport [45].

Principle-based typically fall under local energy deposition. To understand this, consider a point r on a 1D line which represents the photon beam's trajectory to that point. Then, the Batho power law correction factor at the point r can be performed as such where for N different materials above the point r

$$CF(r) = \prod_{i=1}^{N} R_i \times \mathrm{TAR}(x_i)^{(\rho_i - \rho_{i-1}/\rho_0)} \tag{1.13}$$

where $CF(r)$ represents the constant to convert dose known in a homogeneous medium to the dose in a heterogeneous medium, R_i represents the ratio of mass energy absorption coefficients of the ith material and water, TAR represents the tissue-air ratio, x_i the distance in the ith material, and ρ_i the electron densities with ρ_0 being the electron density of water [46]. In the above equation, only the primary photon path is considered, whereas scattered photons and recoil electrons are not considered, so the correction is only based on local energy deposition.

In contrast, some model-based algorithms can calculate non-local energy deposition. Consider two vectors $\vec{r_D}$ and $\vec{r_P}$ that originate at the x-ray source and represent two points in the irradiated volume, where $\vec{r_D}$ represents the point of dose calculation, $\vec{r_P}$ represents the point where a primary photon interacts, and $(\vec{r_D} - \vec{r_P})$ represents a vector starting at point of the primary photon interaction and ending at the point of dose calculation (which will represent the contribution of secondary particles to dose at the point of calculation). Then, the dose predicted a general convolution/superposition method can be calculated as

$$D(\vec{r_D}) = \int_V \mathrm{TERMA}(\vec{r_P}) \times \mathrm{K}(\vec{r_D} - \vec{r_P})\, \mathrm{d}^3\vec{r_P} \tag{1.14}$$

where $D(\vec{r_D})$ represents the dose at point $\vec{r_D}$, V represents the irradiated volume, TERMA$(\vec{r_P})$ represents the total energy released per unit mass at the point $\vec{r_P}$ by primary photon interactions, $K(\vec{r_D} - \vec{r_P})$ represents the fraction of energy deposited at the dose point $\vec{r_D}$ through secondary particles that originate at primary photon interaction point $\vec{r_P}$ (also called the dose spread kernel). The convolution part represents the combining of TERMA and K functions to calculate dose and superposition normally scales K based on physical density at the two points [47]. Together, convolution/superposition algorithms can account for the secondary particles, scattered photons and recoil electrons, that contribute to dose, so non-local energy deposition is considered.

Despite this, convolution/superposition algorithms that only account for physical density can lead to high discrepancies in heterogeneities for kilovoltage beams used in preclinical radiotherapy due to a more pronounced photoelectric effect which has greater dependence on atomic number as discussed in Subsection 1.3.1. This has led to development of Monte Carlo algorithms for more robust preclinical dose calculations. In 2009, a Monte Carlo model of the SARRP small animal irradiator was developed using BEAMnrc Monte Carlo simulation system based on EGSnrc Monte Carlo transport code and validated using EBT film dosimetry with mean absolute percent dose difference of 3.4% along the central beam axis for two collimators (3 mm and 5 mm field sizes) [48]. In 2012, a Monte Carlo model of the X-RAD 225Cx small animal irradiator (discussed in Subsection 2.1.1) was developed also using the BEAMnrc. The modeling of the system's energy spectrum was validated to analytical calculations and 11 collimator geometries (ranging from 1 mm to 40 mm field sizes) to EBT film measurements with a mean absolute percent dose difference of 1-3.2% along the central beam axis (typically increasing at lower field sizes). Then, a cone beam CT

imaging (CBCT) data, which is used for image-guided preclinical irradiations, was interpolated to convert values to material assignment for dose calculations on actual mouse CBCT data [49]. In 2016, a Monte Carlo model of the X-RAD 225Cx was developed using GATE simulation platform based on Geant4 Monte Carlo transport code. The system was validated to film measurements for seven collimators (1-20 mm field sizes) with a mean absolute percent dose different of 1.6% along the central beam axis. Using a variance reduction technique called split exponential track length estimator method, a fast Monte Carlo dose calculation algorithm was developed that reported a speed up factor on the order of 10^3 compared to a full Monte Carlo approach, enabling 3D dose distribution calculations on the timescale of minutes instead of days [32]. A limitation of the study was the focus of dose calculations in homogeneous medium.

These full Monte Carlo models are important for validating faster approaches that could be implemented in preclinical treatment planning software and used for inverse planning. In 2020, this GATE Monte Carlo model was used to validate μ-RayStation (discussed in detail in Section 3.1) which adapted the VMC++ Monte Carlo dose engine used for electron dose calculations for low energy photon dose calculations and smaller voxels. Both models showed good agreement in slab phantom and two murine CBCT cases (thoracic and abdomen) with mean absolute percent dose difference less than 2% in these dose distributions [25]. μ-RayStation can run this VMC++ Monte Carlo dose engine on a GPU to improve computational times. Another GPU-accelerated Monte Carlo dose engine, GARDEN, was validated to Geant4 model of an image-guided small animal irradiator with a mean absolute percent dose difference of around 1% in heterogeneous phantoms and less than 3% in murine two CBCT cases (also thoracic and abdomen) [50]. Further, Monte Carlo models can be im-

portant to understand the dose distributions of more spatially complex radiotherapy treatments such as intensity-modulated radiotherapy and spatially-fractionated radiotherapy. Using a EGSnrc C++ Monte Carlo, grid collimators for the X-RAD SmART with radius of 0.7 mm and center-to-center spacing of 2.4 mm were modeled to simulate preclinical photon grid therapy and validated to film measurements with a mean absolute percent dose difference less than 2% from 0.25 to 3 cm depth in a water phantom [51].

In summary, Monte Carlo is a valuable dose calculation tool for preclinical radiotherapy. Full Monte Carlo dose calculation algorithms act as the gold standard to benchmark other dose calculation algorithms and are incredibly adaptable to any arbitrary geometry setup. Fast Monte Carlo dose calculation algorithms open the door for accurate treatment planning for preclinical radiotherapy experiments. Together, these tools will be valuable in improving translational radiotherapy, and ultimately, the effectiveness of radiotherapy treatments to treat cancer.

1.5 Thesis Goal

The main goal of this work was to evaluate the applications of high-performance computing Monte Carlo (HPC-MC) and GPU-based Monte Carlo (GPU-MC) for preclinical radiotherapy applications, where HPC-MC ran a full Monte Carlo approach and GPU-MC used a fast Monte Carlo approach. The applications explored are discussed below:

1.5.1 HPC-MC

1. **Subsection 2.4.1**: Absolute dosimetry by scaling simulated dose measured by an empirical factor that normalizes dose based on the electronic charge used to generate the primary photon beam in the X-ray tube

2. **Subsection 2.4.2**: Comparative dosimetry by acting as a validation test for other dose calculation algorithms, especially in slab phantoms and CBCT imaging with heterogeneities

3. **Subsection 2.4.3**: Commissioning dosimetry for treatment planning software by importing the energy spectrum, beam modeling, machine geometries, percent depth curves, and lateral beam profiles

4. **Subsection 2.5.1**: Modeling more spatially complex radiotherapy techniques like 3D-conformal and intensity-modulated radiotherapy using 3D-printed objects

5. **Subsection 2.5.2**: Simulating sub-cellular energy deposition to study radiobiological effects

1.5.2 GPU-MC

6. **Section 3.2**: Retrospective treatment planning of preclinical radiotherapy experiments, including those with multimodal imaging and field shaping

7. **Section 3.3**: Comparison of treatment planning techniques including parallel-opposed, static arc, 3D-conformal, and intensity-modulated radiotherapy for image-guided radiotherapy

2

HPC Monte Carlo

2.1 Setup

HPC stands for high-performance computing, which in this case, represents the use of a computing cluster (more precisely, a non-uniform memory access system) to perform rigorous Monte Carlo (MC) simulations using pooled computational resources. The chapter will

cover the development, validation, and application of HPC Monte Carlo (HPC-MC) for preclinical radiotherapy. However first, the geometry and physics of the small animal irradiator modeled for the MC simulation (the X-RAD 225Cx) will be discussed. Then the simulation environment, which used the particle simulator Geant4 and code wrapper TOPAS will be covered.

2.1.1 X-RAD 225Cx

Designed by Precision X-Ray, the X-RAD 225Cx is a fully-shielded cabinet irradiator capable of delivering image-guided and isocentric radiotherapy plans to small animals. The irradiator has a 225 kVp X-ray source and a pixelated CsI detector. The machine can perform cone beam CT imaging and fluoroscopy. For imaging, the machine uses a small focal spot and a 2 mm aluminum beam filter. Using the CT imaging for alignment of the couch, the machine can perform precise treatments to small animals. Generally, collimators can shape the radiation beam on the scale of millimeters at the isocenter, which is the point around which the machine can rotate around for treatments at different gantry angles [52].

At the University of Chicago, five cones are currently commissioned for radiotherapy use ranging from 5 mm to 35 mm nominal field sizes, which represents the beam diameter at isocenter. The interchangeability of the components has allowed for development of a compensator holder that can allow for the insertion of 3D-printed objects to further modulate the beam. Through these 3D-printed compensators, more advanced treatment techniques such as conformal and intensity-modulated treatments can be delivered in a preclinical setting [11, 13]. The ability to perform more advanced radiotherapy in preclinical models will allow researchers to better mimic clinical radiotherapy, and ultimately, the consistency when

transitioning from preclinical to clinical trials is crucial for the success of any translational study.

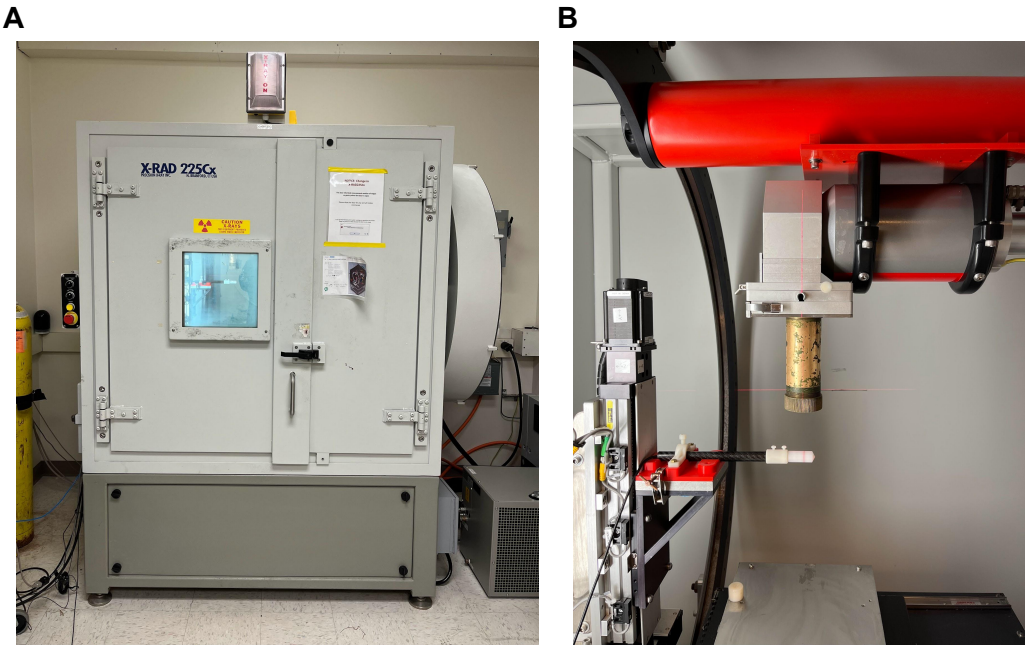

Figure 2.1: X-RAD 225Cx Cabinet Irradiator. The machine is a cabinet irradiator and A) shows the machine with cabinet doors closed during an irradiation while B) shows inside of the machine while the cabinet doors are open during the setup of the irradiation.

2.1.2 Simulation Environment

Geant4 is a toolkit to perform MC simulations of particles through matter developed at CERN [53–55]. Building upon the Geant4 Simulation Toolkit, TOPAS is a code wrapper designed for medical physicists to streamline the use of Geant4 for radiotherapy purposes [56, 57]. The idea was to model all the geometric components of the X-RAD 225Cx that influenced photon generation, collimation, and delivery—starting at the electrons acceler-

ated from the cathode-ray tube. The University of Chicago's X-RAD 225Cx was modeled into geometric components through TOPAS code based on measurements and mechanical drawings where available:

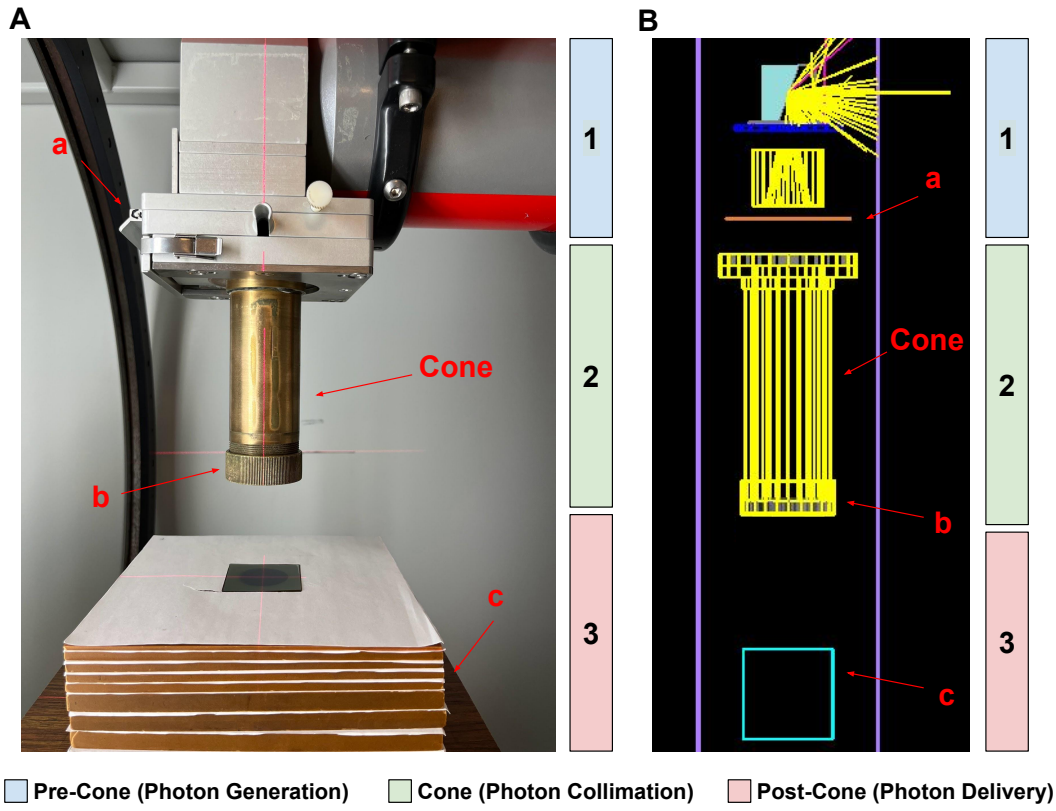

Figure 2.2: HPC-MC Model of X-RAD 225Cx. A) illustrates the delivery of a circular cone to film placed at various depths of a water-equivalent plastic. B) demonstrates an analogous set up in Geant4-TOPAS with a small run of 1000 electrons (in yellow) for visualization purposes colliding into a tungsten target during the pre-cone step. Some components pointed out in both models include a) copper filter, b) cone nut flange, and c) water phantom.

Then, the TOPAS code could be used to run Geant4 MC simulations on the University of Chicago's Radiomics Machine Learning Facility (also known as MEL)—a HPE Superdome Flex NUMA computation server. All simulations performed on this computing cluster used 128 threads from Xeon Gold 6130 CPUs and the most accurate, standard electromagnetic

physics environment from Geant4 (option 4). The scripts developed and used are publicly available on Github.

Instead of creating a single simulation for the entire irradiator, the process was divided into three steps—pre-cone, cone, and post-cone. After each step, only the photons crossing a designated surface were recorded for energy, momentum, and position. The generated file was saved as phase space (.phsp), which then could be imported into future simulations. The modularity helps save computational time. For the propagation through different collimators, the same phase space from the treatment head simulation (step 1 in Figure 2.2) could be used. For the delivery to different phantoms, the same phase space from a collimator simulation (step 2 in Figure 2.2) could be used. Leveraging the hierarchical control of TOPAS, the "Objects" folder stored all the TOPAS code for the geometric components which were called then by an "init" file to set up the simulation. Then, a "submit" file streamlined adjustable parameters such as seed, sequential times, input phase space, electron beam energy, gantry angle, etc. One potential pitfall of a modular setup is the number of files created to run a complete simulation. To document simulations, a shell script "track-submit" recorded the "submit" and "init" TOPAS files along with other salient information like run time and input phase space for any simulation that required an input phase space. Bash scripting was used to automate multiple runs for different cones, phantoms, and gantry angles.

2.2 Propagation

The general physics of the system can naturally be divided into three steps: (1) photon generation, (2) photon collimation, and (3) photon delivery as shown in Figure 2.2. The first step primarily occurs within the X-ray tube, a Comet-MXR 225/22, of the X-RAD 225Cx.

Here, a voltage difference accelerates a beam of electrons to a given energy to collide with an anode target, typically made of some high atomic number material like tungsten. The electrical field of the positive nuclei in the target can decelerate the electrons leading to the release of photons called bremsstrahlung radiation. The photons pass through a circular Beryllium exit window of the x-ray tube, then an opening in the steel house, and a lead primary collimator. Then the beam passes through a metal filter to remove low energy photons that would contribute to scatter and effective dose only in superficial structures of the patient. The X-RAD 225Cx uses 2 mm aluminum filter for imaging and 0.3 mm copper filter for treatment.

In the second step, these filtered beam of photons then pass through a cone (a cylindrical brass component) that does the bulk of the beam collimation. After the filter, the photons first pass through the larger entrance or secondary collimator of the cone made of lead. Then, photons must travel the length of the cone and exit through a narrow final lead aperture, whose dimensions determine the final size of the resulting photon beam at isocenter during treatment (e.g. the nominal 35 mm cone has final lead aperture of 1.295 cm radius). Since the photon beam is diverging, as the distance from the aperture increases, the size of the beam will also increase proportionally. The factor by which the size of beam increases is given by the ratio of the distance from the source to isocenter (SAD) over the distance from source to collimator (SCD). For the X-RAD 225Cx, the proportionality is roughly 1.3 (309 cm / 233.7 cm), thus the nominal 35 mm cone has a diameter of roughly 3.4 cm (1.295 cm radius at 233.7 cm becomes roughly 1.7 cm radius at 309 cm).

Finally, in the third step, the rotational C-arm gantry can deliver the collimated photon beam at any angle converging at a point called the isocenter. The isocenter can be set based on the CT image-guidance and couch translation in all three directions.

The three fundamental physics steps—(1) photon generation, (2) photon collimation, and (3) photon delivery—of the small animal irradiator were respectively mapped into three propagation steps in the simulation named relative to the collimation of the photon beam: (1) pre-cone, (2) cone, and (3) post-cone. These steps for the X-RAD 225Cx and HPC-MC model are juxtaposed in Figure 2.2.

2.2.1 Pre-Cone

The pre-cone step corresponded to photon generation by an electron beam colliding with a high Z anode target to release Bremsstrahlung radiation.

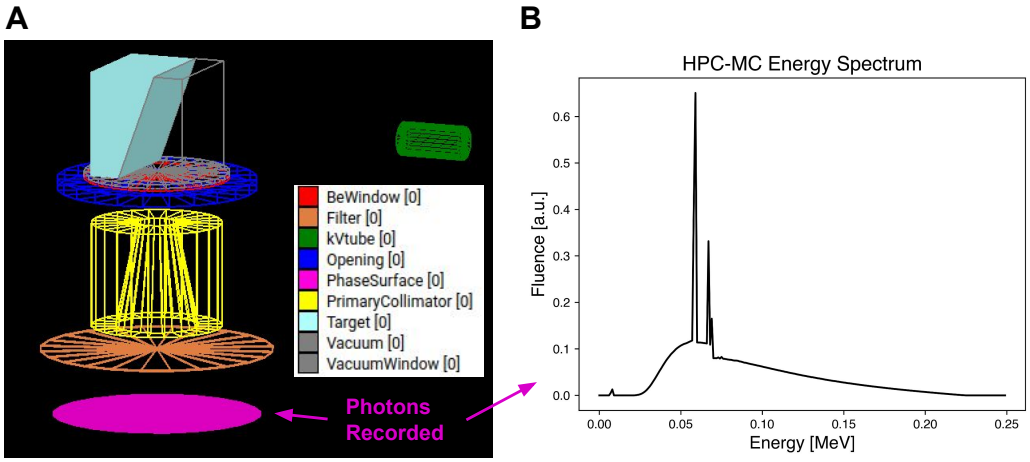

Figure 2.3: Energy Spectrum after HPC-MC Pre-Cone Step. A) illustrates the pre-cone components in HPC-MC model, B) the energy spectrum of 70 million photons that reached the magenta plane at the bottom and were saved in phase space file after a propagation 5 billion electrons.

The Comet X-ray tube was modeled by a square 0.3 mm x 0.3 mm electron beam with a uniform position distribution and beam energy of 0.225 MeV with no beam energy spread. These electrons traveled in a vacuum before colliding with a target anode with an angle of

20 degrees modeled as tungsten right angular wedge trapezoid. The beryllium exit window and opening of the steel house were modeled as cylinders with circular apertures. The lead primary collimator was modeled as a hollow polycone. The filters, 0.3 mm copper and 2 mm aluminum, were modeled as cylinders and were easily interchangeable in the model. A thin cylinder was placed below the filter to record and score the particles that had made it through the pre-cone step. A simulation ran for roughly one week with 90 billion electrons (9E10) and resulted in roughly 951 million photons (9.51E8) with a kinetic energy ranging from 5 to 225 keV. The energy spectrum for 70 million photons from a smaller simulation of 5 billion electrons (9E9) is shown in panel B of Figure 2.3. It would be interesting in the future to model the focal spot's heterogeneous fluence based on the manufacturer's focal spot image provided as done in Chiavassa et al. 2020 [25]. Further, other starting irradiation conditions, such as a 100 kV tube potential without a filter, should be tested to validate HPC-MC model for other energy spectrums and the absolute dosimetry empirical constant derived in Subsection 2.4.1.

2.2.2 Cone

The cone-step corresponded to collimation of photons that were recorded in the pre-cone step phase space. To accomplish this, the phase space produced in the pre-cone simulation, which only contained photons that had reached the surface after filtration and preliminary collimation, was imported as a particle source. The lead entrance aperture (also called secondary collimator), the brass tube of the cone, and a final lead aperture were modeled as cylinders with circular apertures. The photons were collected into another phase space after passing through this final aperture. Five cones commissioned for use at the University of

Chicago's X-RAD 225Cx with nominal field sizes 5 mm, 7.5 mm, 15 mm, 25 mm, and 35 mm were modeled. The fluence after this step of these five cones can be seen in panel B of Figure 2.4.

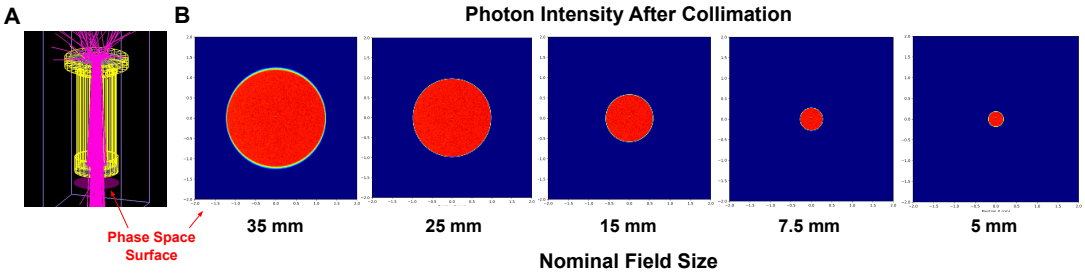

Figure 2.4: Fluence Map after HPC-MC Cone Propagation. A fluence map represents the 2D histogram of photon intensity based on position. A) depicts the simulation of photons through a collimator and then recorded at the magenta phase space surface. B) plots the photon intensity spatially based on a weighted cumulative sum of all the photons in the phase space after propagation through one of the five cones. Note nominal field size is the beam size at isocenter, not at the phase space surface recorded in this figure. Here, the diameters are smaller due to beam divergence.

The 35 mm cone is the main collimator used for preclinical treatments, which is a large field relative to the irradiated tumors. The lead aperture or exit collimator of the 35 mm cone can be swapped with a smaller lead aperture to create a 25 mm cone. For the compensator based deliveries, a compensator holder can be added instead of an aperture. This holder was also modeled in the simulation to enable compensator-based plans in the simulation, as shown in Figure 2.14. A square aperture of 24 mm field size based on an aperture not currently in use was also modeled for the commissioning of GPU-MC, as shown in Figure 2.11. The square aperture was modeled as a TOPAS aperture geometry component, whereas all other circular apertures were modeled as hollow cylinder geometry components native to Geant4. In the future, since the apertures used are not pure lead, the Cerrosafe alloy could be modeled as a new material based on its atomic fraction by weight (Bi $= .425$, Pb $= .377$, Sn $= .113$, Cd $= .085$) and density (9.4 g/cm^3) [58]. Further, it would be interesting to test the

influence of a slanted aperture, which could be modeled as a hollow polycone, to account for beam divergence.

Similar to the pre-cone step, a thin cylinder was placed below the cone and the final lead aperture to record collimated photons that had reached the top of its surface, which is shown in panel A of Figure 2.4. A single propagation of 951 million photons from pre-cone phase space through any of the cones typically took 5-7 hours, and running multiple propagations scaled proportionally. The number of captured photons at the end of the cone increased as expected based on field size (e.g. 21.6 million photons for the 15 mm cone and 98 million photons for the 35 mm cone).

2.2.3 Post-Cone

For this step, the isocentric delivery of the X-RAD 225Cx was modeled by performing three transformations to the phase space produced by the cone step. First, the y-coordinates of the photons, which were all the same since the surface the photons were collected from was orthogonal to the y-axis, were reset by multiplying by zero. Then, they were shifted up such that the isocenter became the center of the simulation (with the x, y, and z coordinates being zero at this point). To account for the capability of rotation by the C-arm for deliveries, a last rotation along the Z-axis axis allowed for a gantry angle to be set for subsequent delivery. A larger 5 cm cube with 0.05 cm cubic voxels was used to model the water-equivalent phantom used in commissioning and measuring of percent depth dose curves. Another smaller 2 cm with .02 cm cubic voxels was used to model the quality assurance phantom used for film measurement of beam modulation treatments.

For the validation of compensator and aperture materials (typically a mixture of metal

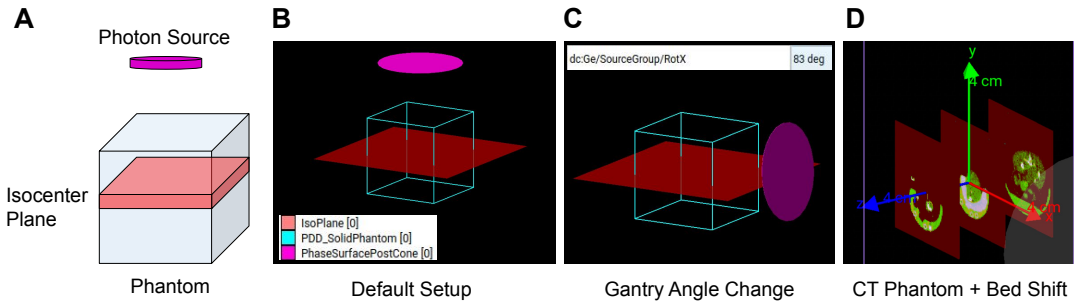

Figure 2.5: HPC-MC Post-Cone Setup. A) represents a simplified diagram of the isocentric post-cone setup, B) illustrates the default setup with a water phantom at 0° gantry angle and without any translation, C) demonstrates the ability to rotate the photon source for deliveries at different angles, and D) depicts the import of CT and conversion to tissue materials given Hounsfield units along with a bed shift and gantry angle change, note photon source and isocenter is respectively shown in transparent gray and as the intersection of the three axes.

and 3D-print plastic) in the simulation, the Radcal Accu-Dose with 10x6-0.6 Ion Chamber with Buildup Cap was modeled. The ionization chamber in the physical and HPC-MC setup is shown in panels A-A' of Figure 2.7 and described in Subsection 2.3.2. Further, the ability to tag different voxels with different materials in TOPAS was leveraged to create heterogeneous slab phantoms. Using a MATLAB script, the size and material of the slab insert could be designed, exported as a .txt file, and then used in the simulation. The slab phantom was used to evaluate another dose calculation algorithm's accuracy in the presence of heterogeneities, which is shown in Figure 2.10. One could also utilize this to create a heterogeneous phantom based on CT volume. A more direct and robust implementation of the CT volumes, but more time-intensive, was performed by the import of DICOM files directly. For dose calculations with a CT volume, two approaches could be performed. One involved the conversion of Hounsfield units to atomic compositions. Another was the use of an RT structure file to map segmentations to a given material. For better comparisons with treatment planning software that might score a dose grid rather than a whole CT, the

RT treatment file could be imported to score only within the dose grid. This could then be saved as another RT treatment file and imported back into the treatment planning system for comparison. Lastly, deliveries may not have rotated on the center of a CT, so the ability to insert bed shifts that move the CT volume in the simulation was added. The set up and some capabilities are shown in Figure 2.5.

2.3 Validation

To ensure the accuracy of the MC model for radiotherapy simulations, two validation tests were performed using (1) film and (2) an ion chamber. Film measurements was used to verify proper modeling of the physical geometries in the HPC-MC model. Ion chamber measurements was used to verify proper material modeling for composite materials not defined elsewhere, such as copper polylactic acid (CuPLA) used in the fabrication of 3D-printed compensators for beam modulation.

2.3.1 Film Measurements

For the first test, film measurements taken at different depths of a water-equivalent phantom in the X-RAD 225Cx were compared to dose-to-medium measurements at the same depths in a water phantom in HPC-MC model for the five commissioned collimators. The results are shown in panel A of Figure 2.6 as percent depth dose curves with dose normalized based on the maximum value.

The beam profiles from the simulation were also compared to the cone's nominal field size, as shown in panel B of Figure 2.6. For the simulation, a 5 cm cubic water phantom

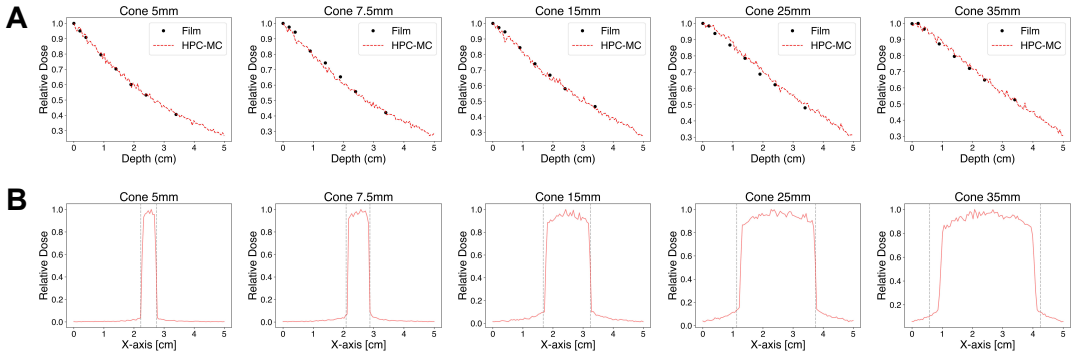

Figure 2.6: HPC-MC Validation to Film Measurements. A) represents the percent depth dose curves along the central beam axis for film measurements and HPC-MC simulations, B) shows the lateral beam profile at isocenter the water cube at a depth of 2.5 cm along the off-center axis and the gray lines represent the nominal field sizes. All values were normalized based on the maximum dose.

was divided into 10,000 of 0.05 cm cube bins using dividable TsBox component. For the percent depth dose curve, the dose at a given depth in the water phantom represented the average of the center four voxels in the cube, which was then divided by maximum of this calculation along the depth of the cube. For the lateral beam profile, a voxel above and below was averaged along an axis at a given depth. The mean percent dose difference of the depth dose profiles for all five cones between HPC-MC and measured data was 2.0% ±0.7%. For the lateral beam profile, the calculated fields sizes (50% of isodose) were on average within 8.30% ±4.76% of nominal field sizes. Some discrepancies were noted before the simulation between the aperture sizes in the blueprints and theoretical magnification factors as discussed in Section 2.2.

2.3.2 Beam Attenuation

For the second test, discs of known elemental material (copper and aluminium) were stacked below the final lead aperture of the 25 mm cone at varying increments and the amount

of dose delivered to ion chamber was measured. The stacked material and ionization chamber is respectively shown by the blue and red box in panel A-A' of Figure 2.7. This served to verify proper modeling of the ion chamber since copper and aluminum had accepted material definitions in Geant4. Accurate results were achieved with a simple three layer geometry of TsCylinder components. The cylinder was a height of 18 mm. From the center to 3.25 mm radially represented the scored volume of ionization chamber (the material G4_AIR was used). From 3.25 mm to 4.5 mm represented the unscored volume of the ionization chamber (again G4_AIR was used). Finally, from 4.5 mm to 7.5 mm was the polyacetal $(CH_2O)_n$ build up cap which used a custom material defined by the known atomic composition of polyacetal by weight (C = 0.4, H = 0.067, O = 0.533) and cited density (1.42 g/cm^3) [59]. The first half-value layer for Cu was 1.04 mm measured and 1.03 mm simulated.

Then, 3D-printed discs of copper polylactic acid (CuPLA) were stacked and measured in a similar manner. For accurate modeling of CuPLA in the HPC-MC model, first polylactic acid (PLA), atomically defined as $(C_3H_4O_2)_n$, was modeled based on cited density (1.25 g/cm^3) and known atomic composition by weight (C = 0.50, H = 0.056, O = 0.444) [60]. Then, CuPLA was modeled as a 4:1 mixture of copper to PLA. Finally, the density of this CuPLA material was set to 3.4 g/cm^3, which was based on the manufacturer's technical datasheet (MetalFil Classic Copper, Formfutura) and empirical corroboration of this value in 3D-prints. This empirical data was used to verify accurate modeling of the compensator material in the simulation. The mean difference in percent beam transmission between measured and simulated for Cu, Al, and CuPLA were respectively 3.39% ±1.12%, 2.09% ±0.80%, and 2.10% ±1.14%. In the future, other materials used to 3D-print beam modulating objects should also be modeled, including the tungsten PLA for conformal apertures.

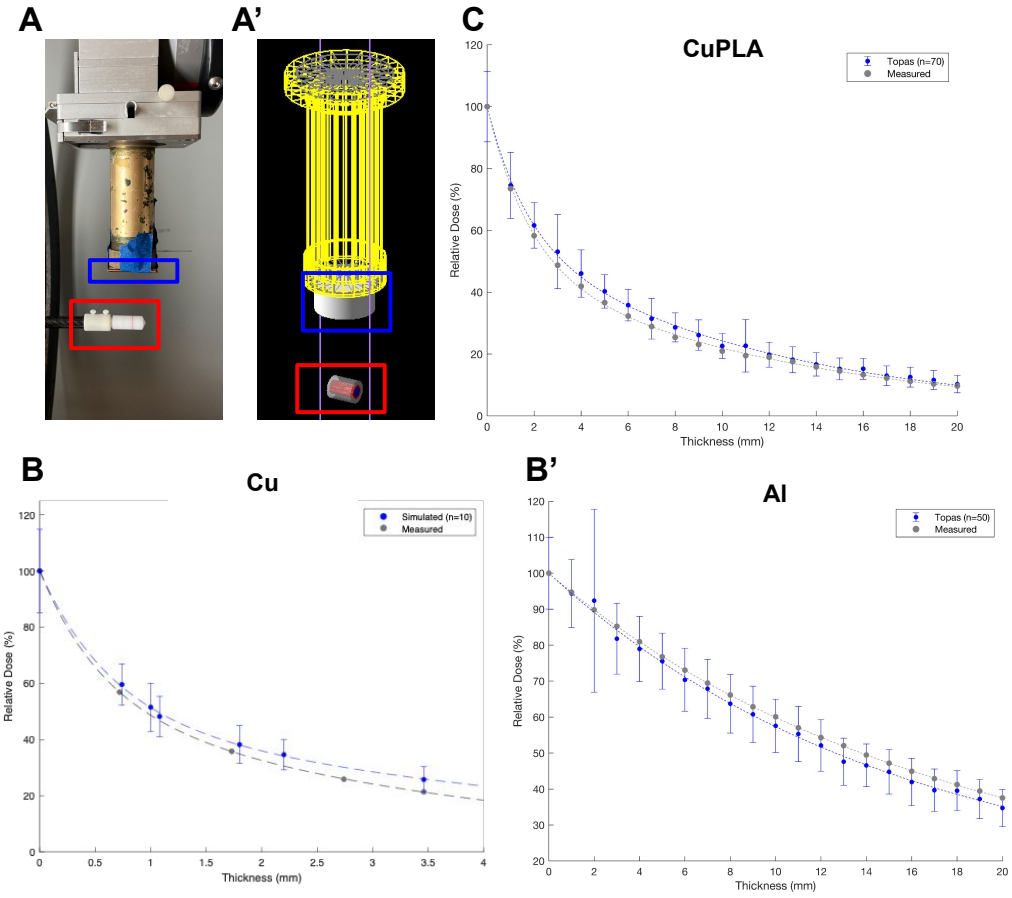

Figure 2.7: HPC-MC Material Modeling Validation. A-A') illustrates the beam attenuation set up where the attenuation material (in blue) and ionization chamber (in red) are highlighted between the two analogous setups, B-B') depicts the beam transmission curve as the thickness of the attenuating material varies for copper and aluminum, which were defined using G4 elemental materials, C) represents the beam transmission curve as 3D-printed discs of copper polylactic acid (CuPLA) used in the fabrication of 3D-printed compensators were stacked below the below final collimator aperture and modeled as a novel material in the simulation. Note the thickness of the attenuating material between A and A' are different in the setups.

2.4 Application

The application of this developed MC model for absolute, comparative, and commissioning dosimetry purposes will be discussed.

2.4.1 Absolute Dosimetry

The absolute doses observed in the model chamber were eight to ten orders of magnitude smaller than that observed in the ion chamber. This was expected since the real system involves a much larger number of particles than the model can reasonably simulate. In the current setup, the energy of the photons produced is determined by the voltage of cathode-ray tube, measured as the kilovoltage peak (kVp), and the intensity of the photons produced is determined by the tube current, measured in miliamps (mA). For preclinical treatments, 225 kVp and 13 mA is typically used for the X-RAD 225Cx. The exposure time, or how long the machine operates at these settings, determines the total dose to the specimen or ion chamber. For a minute long exposure, the following is true about the electrons passing through tube:

$$\text{cumulative electronic charge} = 13\text{mA} \times 60\text{sec} = 780\text{mC} \tag{2.1}$$

Given Faraday's constant ($F = 96485\text{C/mol}$) and Avogadro's constant ($N_A = 6.022 \cdot 10^{23}\text{particles/mol}$):

$$\text{total number of electrons} = \frac{780\text{mC} \times N_A}{F} \approx 4.9 \cdot 10^{18}\text{electrons} \tag{2.2}$$

For scale, the MC simulation running for roughly one week with 128 threads on the computing cluster simulated "only" 90 billion electrons (9E10) across the tube. Hence, such a low dose is reported in the simulation.

However, tracking the number of electrons that contribute to the end dose by tracking dose in terms of gray per coulomb (Gy/C) instead of simply gray can still be beneficial. The feature allows for comparisons between simulations with different number of histories, which will also have intrinsic differences due to noisiness of the simulation. Further, using gray per coulomb will allow for a more meaningful scaling of results to real irradiations. The

observed dose per electronic charge (Θ) was measured for the 25 mm and 35 mm cone at 225 kVp and 13 mA with the 0.3 mm Cu treatment filter and an exposure time of one minute:

$$\text{dose per electronic charge } \Theta = \frac{\text{absolute dose to ion chamber (Gy)}}{\text{current (A)} \times \text{exposure time (s)}} \tag{2.3}$$

$$\Theta(25 \text{ mm measured}) = \frac{2.414\text{Gy}}{0.013\text{A} \times 60\text{s}} = 3.095\text{Gy/C} \tag{2.4}$$

$$\Theta(35 \text{ mm measured}) = \frac{2.479\text{Gy}}{0.013\text{A} \times 60\text{s}} = 3.178\text{Gy/C} \tag{2.5}$$

For calculating the dose per electronic charge, the number of electrons simulated in the pre-cone step was recorded. Prior to the 90 billion electron pre-cone simulation, a 100 billion electron pre-cone simulation was used for certain simulations. The phase spaces were identical in their energy spectrum. A challenge however with using this 100 billion electron generated phase space is that the number of photons generated exceeded one billion, which was the limit placed number of particles able to be simulated by Geant4-TOPAS in a single run, so an extra correction factor (ζ) was required since not all produced photons could be used in subsequent propagation steps. Note these calculations were performed on a larger, older phase space than 951 photon phase space discussed in Subsection 2.2.1. This phase space was also validated in the same manner as done in Subsection 2.3.1, but is no longer in use due to the one billion photon simulation cap. The derivation here will include this extra step of a correction factor as a large amount of simulations scoring dose to ion chamber used this larger phase space:

$$\text{correction factor } \zeta = \frac{\text{usable photons}}{\text{total photons}} = \frac{10^9 \text{ photons}}{1461748775 \text{ photons}} = 0.684 \tag{2.6}$$

$$\text{adjusted electronic charge} = 10^{11}\text{e}^- \times 1.602 \cdot 10^{-19}\frac{\text{C}}{\text{e}^-} \times \zeta = 10.959\text{nC} \tag{2.7}$$

For the simulated ion chamber measurements, the dose per billion photon histories for the 25 mm and 35 mm cone was respectively 37.569 nGy and 38.238 nGy. The 25 mm cone dose

per billion photons was the average over 7 billion photons. The dose per electronic charge for the simulation was the dose per billion photons divided by the electron charge of the pre-cone step:

$$\Theta(\text{simulated}) = \frac{\text{dose per billion photons (nGy)}}{\text{adjusted electronic charge (nC)}} \tag{2.8}$$

$$\Theta(25 \text{ mm simulated}) = \frac{37.569\text{nGy}}{10.959\text{nC}} = 3.428\text{Gy/C} \tag{2.9}$$

$$\Theta(35 \text{ mm simulated}) = \frac{38.238\text{nGy}}{10.959\text{nC}} = 3.489\text{Gy/C} \tag{2.10}$$

Then, the empirical factor (κ) to scale simulated dose results to measured dose results is the measured dose per charge divided the simulated dose per charge:

$$\text{empirical factor } \kappa = \frac{\Theta(\text{measured})}{\Theta(\text{simulated})} \tag{2.11}$$

$$\kappa(25 \text{ mm}) = \frac{3.095\text{Gy/C}}{3.428\text{Gy/C}} = 0.903 \tag{2.12}$$

$$\kappa(35 \text{ mm}) = \frac{3.178\text{Gy/C}}{3.489\text{Gy/C}} = 0.911 \tag{2.13}$$

For another experiment, the same setup of the tube potential, tube current, copper filtration, and ion chamber was performed at larger exposure times for absolute dose measurements with the 35 mm cone. For longer exposure times ($>$ 300 seconds), the dose rate converged to 3.141 Gy/C, a slightly lower value than measured at 60 seconds. Recalculating the empirical factor for the 35 mm cone yields

$$\kappa^*(35 \text{ mm}) = \frac{3.141\text{Gy/C}}{3.489\text{Gy/C}} = 0.900 \tag{2.14}$$

This suggests $\kappa \approx 0.9$ in general, though lower field sizes would have to be tested to confirm this. Further, there is on average a 10% percent error between the measured and simulated dose per charge. Despite the low conversion of photon energy into deposited dose in air leading to high noise in simulated ion chamber measurements, the similarity across trials

with a large number of histories pointed away from noise, particularly in the dose scoring of the air volume in the post-cone step. Although some of the error may be explicable to the modeling of ion chamber in the simulation, another possible explanation could be the ideality of simulation in the pre-cone step. In the MC model, electrons are accounted for and precisely slammed in the focal spot for the generation of photons. In reality, the tube has a focused electron beam with an electric field, but some will stray off focus and not contribute equally to the photons generated. The measurement of tube current is also more difficult than counting simulated electrons and can very slightly over the duration of the delivery.

Further, the tube must ramp in and there is known correction factor to account for the system's response time, known as the end-effect. To evaluate the contribution of this effect, exposure time was varied at ten points from 1 s to 600 s and absolute dose delivered to an ion chamber was measured. The exposure time versus absolute dose was fit linearly to assess for non-linearity:

$$\text{exposure time (s)} = a \cdot [\text{absolute dose to ion chamber (Gy)}] + b\,\text{s} \tag{2.15}$$

$$f(x) = ax + b = 24.5\frac{\text{s}}{\text{Gy}} \cdot x - 1.05\text{s} \tag{2.16}$$

Ideally, dose should be linearly proportional to exposure time. So, the end-effect represented the contribution of the constant term b in a linear equation. In this case, this contribution was -1.05 seconds. Dose rate strictly decreased as exposure time increased before converging to 2.45 Gy/min after 300 seconds. Dose rate per second by linear fit was 0.0407 Gy/s, so a discrepancy of 1 second is negligible, especially for deliveries over the time scale of minutes. In 60s exposure, a 1 second discrepancy could account for $1.\overline{6}\%$ difference, but given the the contribution of the end-effect was a negative time, this would move the empirical factor away from 1. A potential flaw could be the accuracy of the ion chamber at low

exposure times of 1, 3, 5, and 15 seconds which seems to overestimate dose, but recomputing the linear fit omitting those values yields -1.01 seconds. Calculated dose rate per minute for times 30 seconds and greater varied by less than 4%. Given this data, it seems a large part of the discrepancy between dose per electronic charge measured versus simulated could be due to a non-ideal focus of the electron beam in the cathode tube onto the target. Empirical ion chamber measurements on the X-RAD 225Cx based on varying irradiation time and tube current are summarized in Figure 2.8.

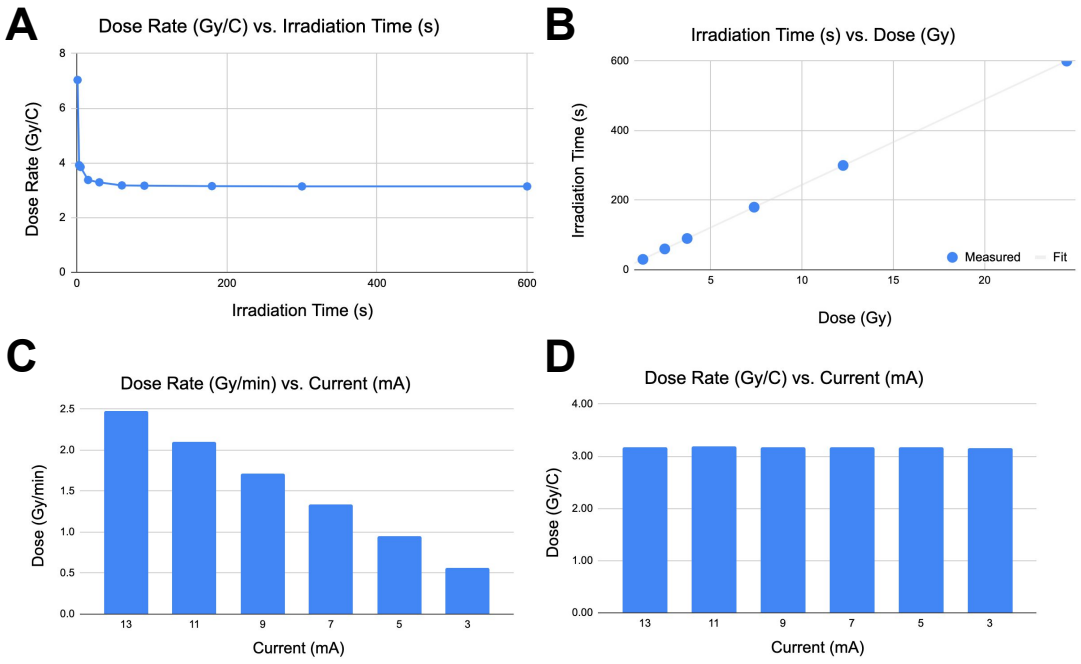

Figure 2.8: X-RAD 225Cx Ion Chamber Measurements. A) depicts the dose rate per electronic charge over irradiation time, B) shows the irradiation time as a function of dose where the x-intercept of the fit represents the end-effect correction, C) illustrates dose rate per minute as a function of current, D) depicts the equality of dose rate between different currents when normalized into dose per electronic charge.

2.4.2 Comparative Dosimetry

For the fabrication of apertures and compensators used in more complex treatment plans, dose calculation algorithms need to minimize computational speed to be preclinically feasible. After only all the imaging of the mouse is completed, can these components be fabricated. The isocenter is aligned by the CT imaging in the X-RAD 225Cx while the mouse anesthetized, and the goal is to fabricate these beam-modulating components as rapidly as possible after this imaging. For this purpose, the long computational times of a full MC approach limit its application for designing these components. Typically, simulations are repeated to perform inverse treatment planning that optimizes a treatment given an objective function. However, faster dose calculation algorithms require approximations to achieve the desirable computational speed, so the MC model can be used as an accuracy test for these faster algorithms.

At the University of Chicago, the fabrication of compensators for small animal intensity-modulated radiotherapy uses an open-source pencil beam dose calculation algorithm MatRad for inverse treatment planning [11, 61]. The version has been modified to use MC-generated dose kernels for a 225 kVp treatment beam, but the treatment planning system uses a pencil beam algorithm to determine final doses in CT voxels. The pencil beam algorithm accounts for the density-dependence of photon attenuation and dose absorption through converting the Hounsfield units of the CT volume into electron density based on a lookup table.

A problem with this approach, especially at lower energy levels, is the introduction of the photoelectric absorption as a competing ionizing radiation interaction to Compton scatter-

ing discussed in detail in Subsection 1.3.1. The probability of Compton scatter is dependent on photon energy, but nearly independent of effective atomic number, thus electron density alone can accurately approximate the cross section of Compton interactions. In contrast, the probability of the photoelectric effect is dependent on both photon energy and effective atomic number to the third power. Thus, a pencil beam algorithm often suffers in accuracy around heterogeneous regions even after density adjustments, and this inaccuracy would be particularly exacerbated in the presence of higher Z materials at lower energy ranges.

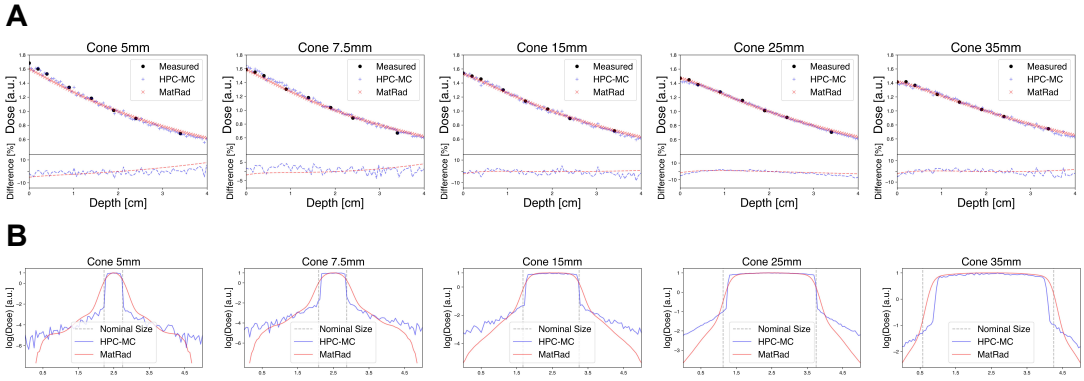

Figure 2.9: MatRad Validation to Film Measurements and HPC-MC. A) illustrates the percent depth dose curve of MatRad (red), HPC-MC (blue), and film (black), B) represents the lateral beam profile of MatRad (red), HPC-MC (blue), and nominal field size (grey). Depth dose curves were normalized to dose at 2 cm depth and lateral beam profiles were normalized to integral of depth dose profiles and logarithmically scaled.

To assess the level of inaccuracy around heterogeneities, identical treatments to slab phantoms were setup between the pencil beam (PB) and the Monte Carlo (MC). But first, the pencil beam simulation was compared to film measurements and HPC-MC simulation for accuracy of dose calculation in a water phantom analogous to the validation of the MC model in Subsection 2.3.1. The mean percent dose difference between film and the pencil beam was $2.9\% \pm 1.1\%$. Cone sizes were not based on modeling of collimators but instead a filter-

ing of photons within a radius that represented the nominal field size. The results are shown in Figure 2.9.

For the slab phantom design, a 5 cm cube was divided into three layers with the top and bottom layer being tissue and the middle layer (the insert) being 5 mm insert of a material of choice as shown in panels A and B of Figure 2.10. A solid tissue phantom without an insert acted as a control. Material of air, bone, and cortical bone were used as an insert. For the MC simulation, a material definition required an atomic composition and physical density (g/cm^3). For the pencil beam simulation, a material definition required the electron density ($e-/cm^3$). Since the two simulations required different parameters to define materials, careful attention was made to ensure both treated a given material as similarly as possible. The end definitions are shown in table below:

Materials	g/cm^3	Monte Carlo (NIST-defined)	Pencil Beam
Tissue	1.127	G4_A-150_TISSUE	1.12
Air	0.0012†	G4_AIR	0†
Bone	1.45	G4_B-100_BONE	1.38
Cortical Bone	1.92	G4_BONE_CORTICAL_ICRP	1.78

Table 2.1: Material Definitions for Slab Phantom. NIST-defined materials can be identified on the Geant4 Material Database for the exact atomic composition [62]. Relative electron density to water was for these selected materials was determined based on the conversion from density using the lookup table. †Note for air the physical density is rounded here but not in the simulations and the electron density was based on the lookup table conversion of -1000 HU to electron density.

First, materials were selected from the Geant4 Database of NIST compounds. These materials had known densities and atomic compositions. A-150 and B-100 represent respectively a tissue-equivalent and bone-equivalent plastic. Cortical bone was defined as suggested based on ICRP guidelines [62]. The relative electron densities to water for these materials was based on the conversion from density using the lookup table.

To construct the phantom in for the pencil beam simulation, a 3D array in Matlab was modified with desired values. For the MC simulation, individual voxels were set to the desired material using a text file generated from the conversion of Matlab 3D array into the format specified by TOPAS `Ge/.../VoxelMaterials` parameter. A Matlab script was developed to automate the creation of this text file such that slab phantoms of different thicknesses and materials could be developed by inputting the desired parameters. There was agreement in the tissue with a mean dose difference within 2%, whereas the mean dose difference after the insert was -1.3%, 9.7%, and 17.7% for air, bone, and cortical bone respectively. The results suggest the pencil beam simulation has good agreement in water and soft tissue but substantial differences arose in bone inserts, especially in the denser cortical bone, as shown in panel E of Figure 2.10.

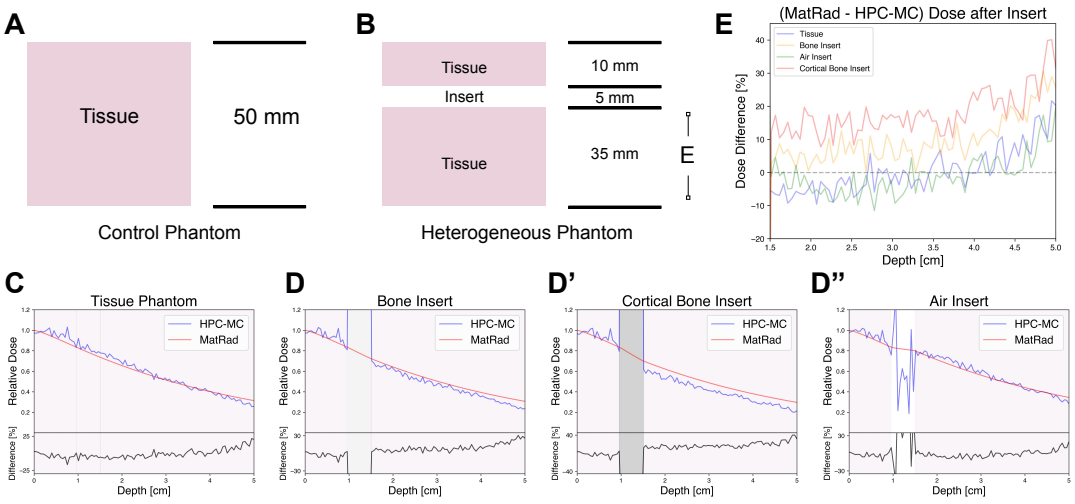

Figure 2.10: HPC-MC and MatRad Slab Phantom Comparison. A) shows the control homogeneous phantom without any insert, B) shows the heterogeneous phantom with a 5 mm insert at 1 cm depth, C) depicts the depth dose curve in the control phantom, D-D") depicts the dose curve in the slab phantoms with the insert material region shaded, E) illustrates the dose difference between MatRad and HPC-MC after the insert. Note dose difference was always calculated as MatRad dose subtracted by HPC-MC dose after normalization.

2.4.3 Commissioning Dosimetry

μ-RayStation (Micro-RayStation) is a preclinical treatment software built upon the clinical treatment software RayStation 8B, developed by RaySearch Laboratories (Stockholm, Sweden) discussed in detail Section 3.1. The system uses a fast GPU-based MC approach which makes a couple approximations to achieve dose calculations on the timescale of minutes rather than hours or days as required for HPC-MC in Geant4-TOPAS. For the commissioning of the system, a percent depth dose of a square reference field must be used. However, at the University of Chicago, only circular collimators are used. So, an old square reference field not currently commissioned was found and film measurements were taken in a water phantom. However, there was some problems encountered with film measurements due to potentially different batches films being used and/or a previously undocumented contamination of the film used.

So instead, the aperture of the square reference field was modeled the MC simulation using a TsAperture geometry, a specialized component in TOPAS which allows for a polygonic aperture based on inputted (x, y) coordinates. A fluence map of the phase space right below the square aperture was calculated to verify proper field shaping. MC simulation of the square field into a water phantom was performed identical to Subsection 2.3.1. In total, over three billion photons (3.275E9) were scored in a 5 cm water cube divided into 10,000 voxels for the percent depth dose and lateral beam profile curves. The dose plane at isocenter orthogonal to the beam was calculated to further confirm a square field was delivered. Then, all the machine parameters were set based on the same data used to build the (HPC-MC) model.

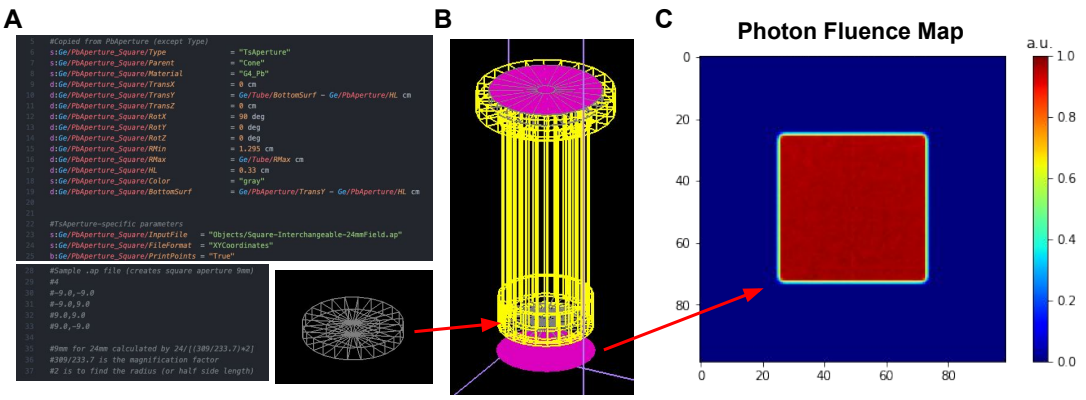

Figure 2.11: Square Aperture for μ-RayStation Reference Field. A) a square aperture was modeled using a TsAperture specialized component, B) photons were propagated through the cone with this aperture, C) a fluence of the photons passing through the magenta plane verified the rectangular field shaping.

For beam modeling, the primary electron beam source matched the HPC-MC model electron beam in size and distribution. An energy spectrum based on roughly 70 million photons (7.07E7) was also imported from the HPC-MC model based on the phase space produced in the pre-cone step. This was a smaller than the pre-cone phase space used for propagation since processing the larger phase space was too computationally expensive for Jupyter Notebook run on the computing cluster. Since the electron beam was orthogonal to the photon beam axis, the flattening filter weight was set to 0. To determine the monitor units per second (MU/s) of the machine, the dose rate at 13 mA and 225 kVp with a 0.3 mm Cu filter was found to be 2.45 Gy/min, which was 4.08 cGy/s. The absolute dose calibration point was set such that dose per monitor unit was 1 cGy per 1 MU, thus the steady dose rate was 4.08 MU/s. The output factor when importing the 35 mm cone data was calculated to be 1.0244 based on the following equation:

$$\text{Output Factor for 35 mm Cone} = \frac{\text{Dose at 1cm for 35 mm Cone}}{\text{Dose at 1cm for 24 mm Reference Field}} \tag{2.17}$$
$$= 1.0244$$

All the following salient machine parameters modified to commission the University of Chicago's X-RAD 225Cx in μ-RayStation are listed below:

Machine Parameter	Value
Source-Axis Distance (SAD)	30.7 cm
Reference Field Size	2.4 cm × 2.4 cm
Block Tray Position	23.6 cm
Entrance Collimator Position	9.2 cm
Secondary Collimator Position	22.8 cm to 23.6 cm
Electron Beam Size	0.4 cm × 0.4 cm
Electron Beam Distribution	Uniform
Dose Rate	4.08 MU/s
Output Factor (for 35 mm)	1.0244

Table 2.2: Machine Parameters for GPU-Based Monte Carlo Model. Source-Axis Distance (SAD) represents the distance separating the radiation source and the isocenter axis. The reference field was chosen based on the size of the old aperture found and modeled in the HPC-MC model. The block tray distance was the distance from the source to the compensator/aperture holder insert. The entrance collimator and secondary collimator corresponded respectively to the collimator for photons entering the cone and the final aperture of the cone that determined field size.

The percent depth dose and lateral beam profile in a water phantom was compared between the HPC-MC model and μ-RayStation in analogous setups for the 2.4 cm × 2.4 cm reference field and 35 mm cone. The results for the reference field are shown in Figure 2.12. For both collimators, the mean dose difference for the percent depth dose curves was within 1%. The lateral beam profile of the reference field matched within 2%. The 35 mm cone lateral beam profile from the HPC-MC model was slightly smaller than the μ-RayStation, but it noted that the nominal 35 mm cone was slightly small in diameter, thus the small deviation around the edge of the field between the two models was expected.

In the future, the 35 mm cone will be adjusted to 34 mm in μ-RayStation for better agree-

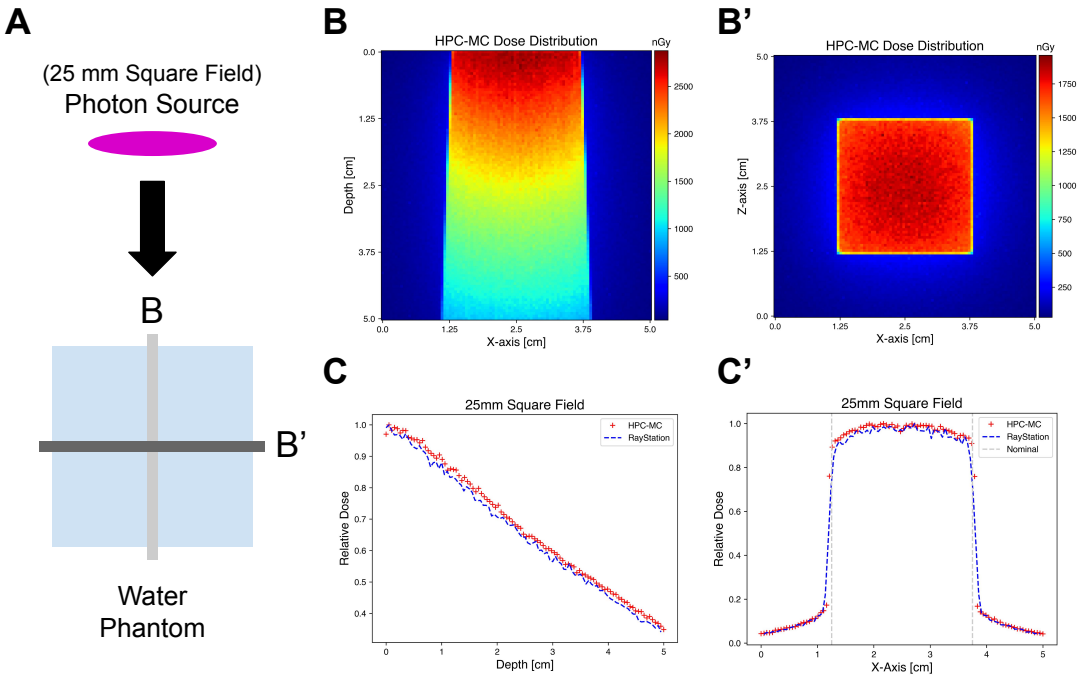

Figure 2.12: μ-RayStation Validation in Water Phantom. A) represents a simplified diagram of the irradiation setup, B-B') shows the 2D dose distribution along central beam axis and off-center beam axis, C-C') demonstrates the agreement between the HPC-MC (red) and Micro-RayStation (blue) in both axes.

ment with the HPC-MC model, but since the 35 mm cone was used for large field irradiations for coverage with no targeting (for scale, the treatment volume taken in the CT step is also about 35 mm), the following deviation would be negligible for the retrospective analysis discussed in the next chapter. Additionally, the other four cones will also be modeled and validated in an analogous fashion. Python scripts were used to automate import of HPC-MC data into the RayPhysics module of μ-RayStation.

2.5 Future

2.5.1 Beam Modulation Treatments

Through the material modeling of CuPLA in Subsection 2.3.2, more complex treatment plans beyond circular cones could be simulated. CuPLA is the material used to 3D-print compensators, which can be used to deliver intensity-modulated radiotherapy treatments in small animals [11]. The open-source pencil beam dose calculation algorithm Ma-

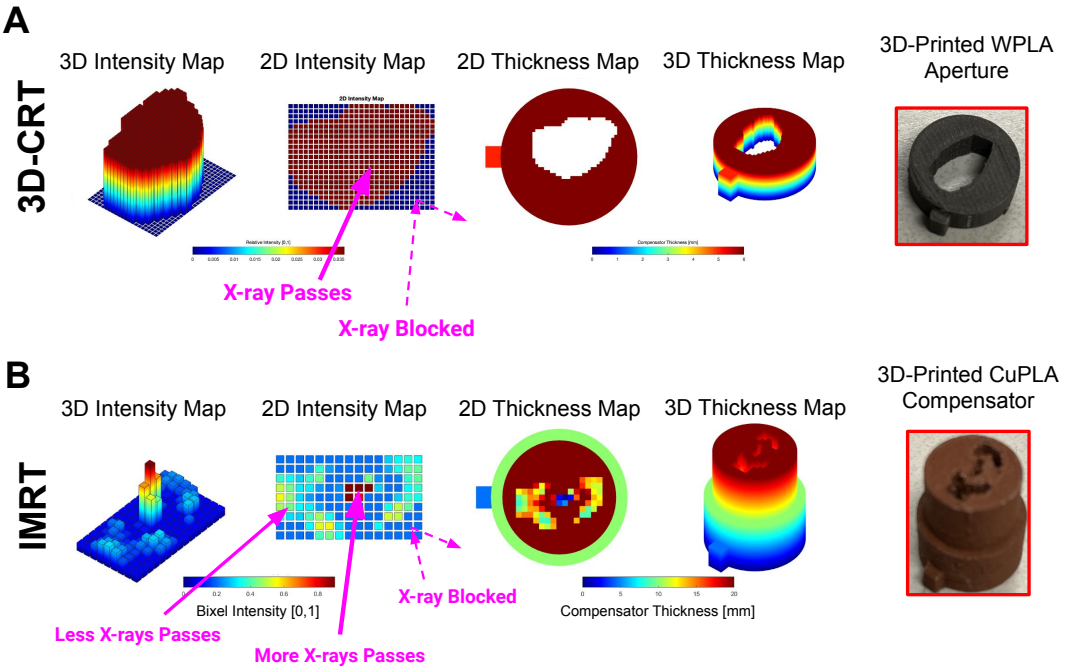

Figure 2.13: Compensator-Based Treatments in HPC-MC. A) demonstrates the intention of binary passing or blocking of 3D-printed tungsten PLA apertures, B) illustrates the intention of modulation of X-ray intensity across a grid using 3D-printed copper PLA compensators.

tRad evaluated in Subsection 2.4.2 designs these compensators by inverse planning optimizing of bixel intensity weights. WPLA (tungsten PLA) is also used to 3D-print apertures

for conformal radiotherapy [13]. Beam modulation treatments using these 3D-printed objects is shown in Figure 2.13.

To use 3D-printed objects, the final aperture in the cone was replaced with a tungsten PLA compensator holder as shown in the top of panel A of Figure 2.14. The holder was first imported as an STL, but due to performance and step error issues, it was modeled with TOPAS cylinder primitives. Then, the 3D-printed compensator could be imported as an STL object in the simulation. Beam modulation was verified by a fluence map after a cone propagation through the compensator-holder geometry and then a post-cone propagation into a water phantom. For multi-angle treatments, bash scripts were developed to automate gantry angle and compensator changes. Current work is underway to use the HPC-MC to validate the compensator designs developed using MatRad by comparing 3D dose distributions in a water phantom and murine CT cases. A 3D-conformal dose distribution can be seen in Figure 3.1 of the GPU-MC chapter.

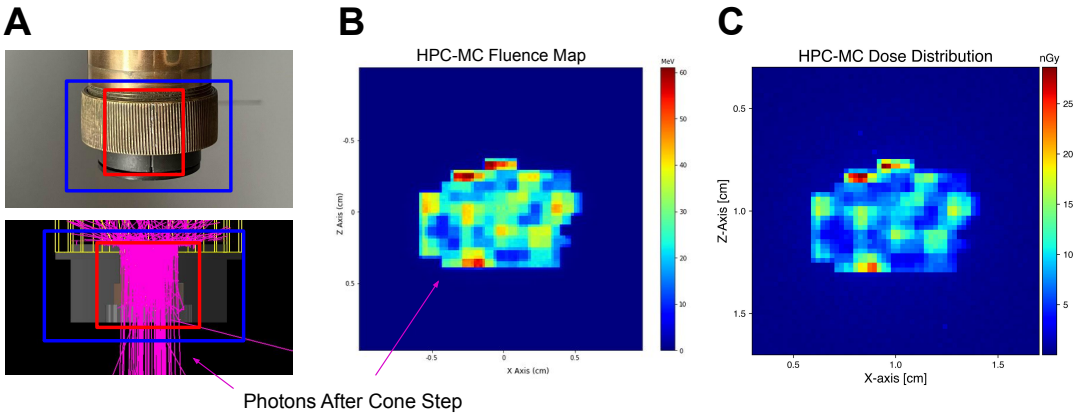

Figure 2.14: Compensator-Based Treatments in HPC-MC. A) demonstrates the tungsten PLA compensator holder (in blue) and copper PLA compensator (in red) in the X-RAD225 Cx (top) and in HPC-MC model (bottom) with photons shown as magenta, B) illustrates the fluence of the phase space after beam modulation through the cone, and C) demonstrates the dose distribution at isocenter orthogonal to the beam axis in a water phantom.

2.5.2 Multiscale Treatments

The main purpose of radiotherapy is to treat and kill cancerous tissue. Thus, it is important to not only study radiotherapy at the macroscopic level of dose distributions in structures but also the radiobiological consequences at a sub-cellular level. Cell death from radiation exposure occurs primarily through DNA double-stranded breaks. Further, exposure to ionization radiation causes the activation of certain genetic pathways involved in DNA repair [63]. Fundamentally, ionizing radiation induces cellular and sub-cellular response, and cell death becomes a consequence of these biological mechanisms. The ability to connect these cellular mechanisms to macroscopic observations is important for understanding the interplay of oxygenation, radiosensitization, genetic pathways, and other biological factors with radiotherapy. TOPAS-nBio, an extension of TOPAS, enables radiotherapy simulations at the nanometer scale on sub-cellular components like DNA, mitochondria, chromatin fiber, and other biologically salient structures [64]. Currently, work is being done to scale down fluence of the phase spaces from macroscopic MC models of the two major cabinet systems down to the cellular level. Using this scaled down phase space, future work is looking at delivering these photons to an ellipsoid cell within a MOBY mouse phantom, modeled in TOPAS-nBio, to calculate DNA damage.

3

GPU Monte Carlo

3.1 μ-RayStation

μ-RayStation is clinical treatment planning software adapted for preclinical radiotherapy. The software is able to perform fast GPU Monte Carlo (GPU-MC) calculations to calculate dose distributions within minutes rather than on the order hours and days required for

full Monte Carlo models. The commissioning of the system to the University of Chicago's X-RAD 225Cx small animal irradiator is discussed in Subsection 2.4.3. The GPU-MC simulations were run with a NVIDIA Titan X Pascal 12 GB GPU.

3.1.1 Background

RayStation 8B is a clinical treatment planning software developed by RaySearch Laboratories (Stockholm, Sweden) with the capability to perform photon, electron, and proton therapy and plan state of the art radiotherapy techniques like volumetric modulated arc, intensity-modulated, and 3D-conformal radiotherapy. The software has all features expected of clinical treatment planning software such as multi-criteria plan optimization, deformable registration, segmentation tools, and efficient dose computations. μ-RayStation adapts this clinical software for a lower energy and sub-millimeter voxel sizes required for preclinical radiotherapy. μ-RayStation leverages the VMC++ Monte Dose engine used for electron dose calculation in the clinical software, and repurposes this for low energy photon beams used in small animal radiotherapy [25]. VMC++ is a fast and accurate voxel-based Monte Carlo approach which had been redeveloped in C++ with some improvements for variance reduction and modeling of physics [65]. The approach has been validated for photon beams from 20 to 1000 keV, thus it has been validated at preclinically relevant energy ranges [66].

3.1.2 Approach

For μ-RayStation, three assumptions were made in the model: (1) a photon with a path intersecting a collimator is completely absorbed, (2) irradiator-generated scatter is negligible, and (3) the heel effect along with other factors that might cause energy or fluence hetero-

geneity due to source direction is negligible. The three main components of the model then became the source, entrance collimator, and exit collimator. Three main parameters required to model a photon were the energy, position, and direction. Using the source probability distribution, a photon's initial position was sampled. Then, given the geometry of the exit collimator, the photon's final position was sampled. These two points are connected and only if it does not intersect the entrance collimator is the photon considered viable and included in the simulation. The approach was validated to film and a full Monte Carlo model built in GATE running Geant4 Monte Carlo transport code in a water phantom. Further validation to the GATE approach was done in slab phantom and a murine CBCT volume. To improve calculation time, a validated split exponential track length estimator method was employed, decreasing computational on the order of 10 to 100-fold to the full Monte Carlo model with a maximal dose difference of 2% in the tumor of the murine CBCT case. The Chiavassa et al. 2020 paper can be referred to for a more detailed overview of the setup of the software and validation of the dose calculation algorithm [25]. In the following chapter, μ-RayStation will be used to perform a retrospective planning of a preclincal radiotherapy experiment and evaluate prospective treatment techniques.

3.2 Retrospective Planning

Using μ-RayStation's GPU-MC, five cases in an oxygen-guided preclinical radiotherapy experiment was retrospectively planned. The goal of the experiment was to assess the benefit a targeted increased dose to the hypoxic region of the tumor in a preclinical model. Tungsten PLA apertures were 3D-printed based on imaging of tumor using magnetic resonance imag-

ing (MRI) and of oxygenation levels using electron paramagnetic resonance oxygen imaging (EPROI). These apertures were used to perform 3D-conformal radiotherapy that delivered an equivalent boosted dose to either the hypoxic or oxygenated (non-hypoxic) region of the tumor. Survival outcomes of the mice were measured over the course of 180 days. Gertsenshteyn et al. 2023 paper can be referred to more comprehensive details of the experiment [14]. The purpose of the work here was to evaluate GPU-MC treatment planning software to plan, deliver, and retrospectively analyze 3D-conformal treatments in mice.

The first step was to import the imaging data into μ-RayStation. Imaging data, including registered CBCT, MRI, and EPROI for 5 mice with SCC7 squamous carcinoma leg tumors were imported using 3D Slicer. For the export of imaging from 3D Slicer, the open-source extension SlicerRT was used [67]. The MRI and EPROI were exported as a DICOM scalar volume from 3D Slicer. The CBCT was exported with the segmentations, which included the tumor and hypoxia contours, as a DICOM-RT patient. Then, the treatment data was imported into μ-RayStation. Treatment data included gantry angles, irradiation times, bed shifts, and conformal apertures. For import of apertures, a magnification factor was applied to scale the contour for import. Python scripts using a CPython 3.6 interpreter in μ-RayStation were created to automate the import of imaging and treatment data.

Experimental treatment plans were designed to deliver 48 Gy whole tumor (base) dose and 13 Gy boost dose. The 13 Gy boost dose was delivered by parallel opposed 3D-printed tungsten PLA conformal apertures. The five cases analyzed treated hypoxic regions ($pO_2 \leq 10$ torr) as the boosted volume. Experimental apertures were derived from a 1.2mm expansion of hypoxic segmentation in the beam's eye view (BEV). Boost beam angles were optimized for hypoxic area compactness in BEV based on sampling of 5 equiangular beams. For the

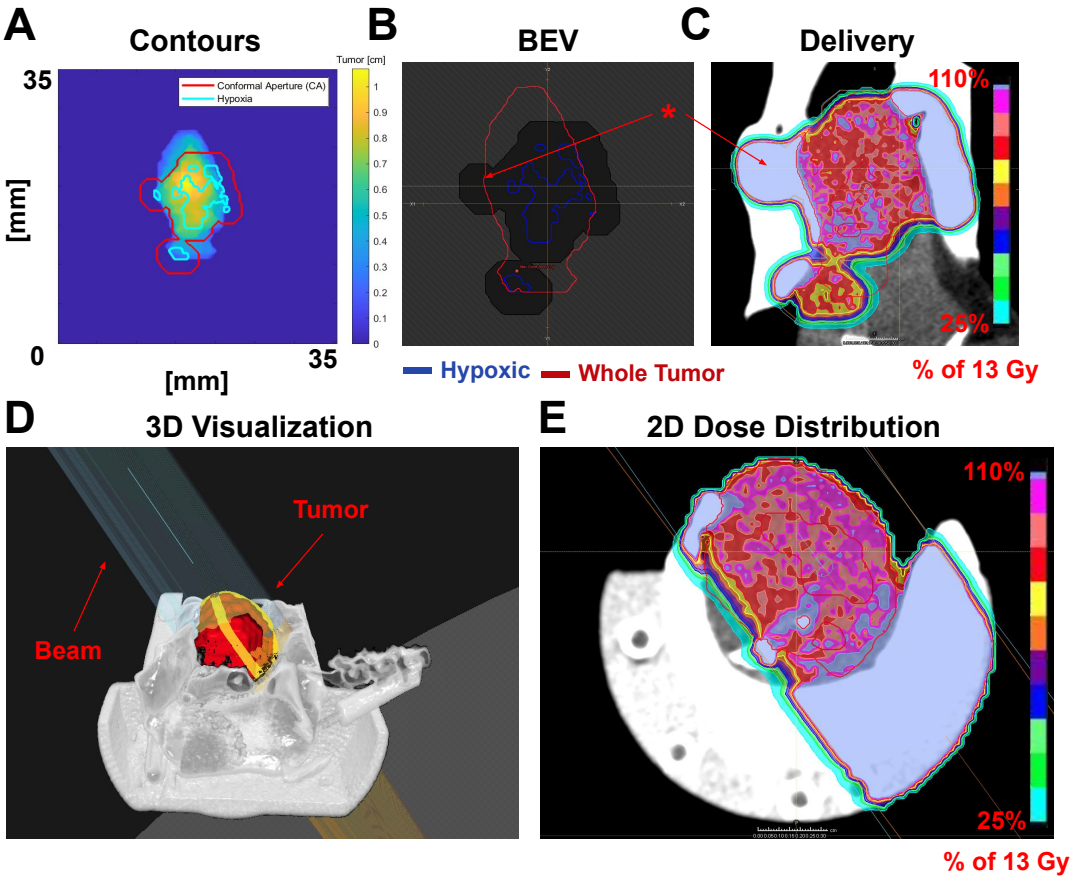

Figure 3.1: Import and Delivery of Conformal Aperture Contours. A) plots the tumor thickness in the beam's eye view (BEV) with the conformal aperture contour (in red) and hypoxia contour (in blue), B) illustrates the BEV in μ-RayStation after importing the conformal aperture contour, C) depicts the dose distribution on a slice after delivery of the conformal aperture (which was at an angle, hence the horizontally stretched aperture shape in the dose distribution), D) illustrates the 3D beam arrangement of the parallel opposed 3D-conformal treatment, E) represents the dose distribution on a slice orthogonal to panel C. Note the red asterisk marks segmentations that were thresholded out to remove high HU regions that overlapped onto high-density immobilization material around the leg but no changes were made to imported conformal apertures. Further, the aperture contour imported contained the 1.2 mm margin added to the hypoxic boost aperture around the hypoxic region, as stated in Gertsenshteyn et al. 2023 [14].

base dose, 35 mm parallel opposed circular beams were delivered, however, experimental lead shielding commonly used to protect non-target regions was not modeled.

On average, the hypoxic target volume (HTV) was 49 mm^3 and 10% of the tumor vol-

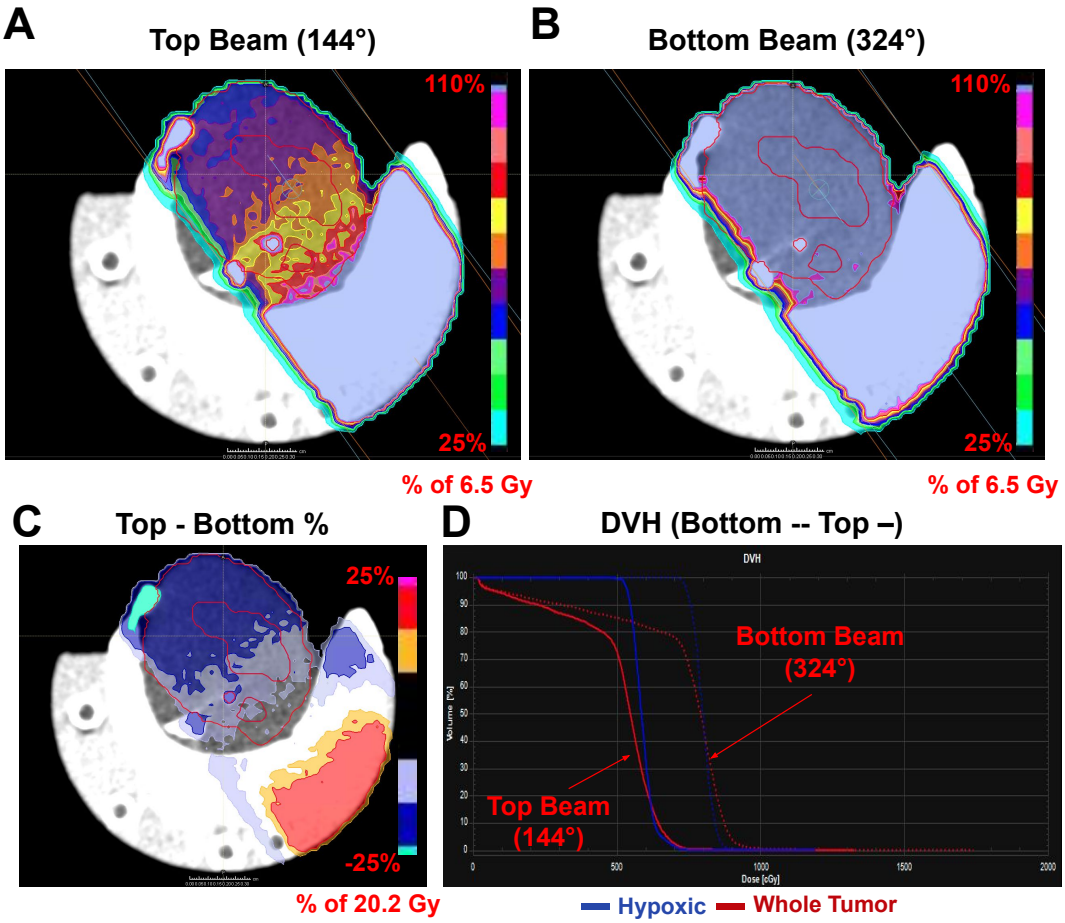

Figure 3.2: Parallel Opposed 3D-Conformal Beams with Irradiation Times. A) illustrates the dose distribution for the top beam at 144 degrees with an irradiation time of 169.76 seconds (692.62 MU/fx), B) shows the dose distribution for the bottom beam at 324 degrees with an irradiation time of 198.07 seconds (808.13 MU/fx), C) represents the dose difference in percent between the top and bottom beam, D) presents the dose-to-volume histogram for top (solid) and bottom (dashed) beams in the hypoxic (blue) and oxygenated (red) structures.

ume. The HTV V_{61Gy} (the percent of the volume receiving 61 Gy) and $D_{98\%}$ (the minimum dose that 98% volume received) were respectively 87.2%±8.2% and 59.4 Gy±1.3 Gy. The $D_{98\%}$ difference between the HTV and non-HTV was 10.5 Gy±1.4 Gy. Total tumor volume receiving the total base+boost dose (61 Gy) was 69.1% ± 12.4%. Preliminary results suggest integration of μ-Raystation, and more generally 3D treatment planning soft-

ware, into the workflow of preclinical radiotherapy experiments could be useful, especially for image-guided and beam modulation treatments. A larger 31 case cohort with boost dose to the hypoxic region in 16 cases or oxygenated (non-hypoxic) in 15 cases has been performed. The next step is to analyze the dose distributions, dose metrics, dose-volume histograms, and hopefully began connecting this information to the treatment outcomes of these mice. Concurrently, it would be interesting to compare the 3D-conformal deliveries between the HPC-MC and GPU-MC models to assess the accuracy of the fast GPU dose calculation algorithm for beam modulation treatments, which has yet to be done.

3.3 Treatment Comparison

Small animal intensity-modulated radiation therapy (IMRT) has been a recent advance in preclinical radiotherapy with the potential for more precise treatments than 3D conformal radiation therapy (3D-CRT) and static arc therapy (SAT). The purpose of this work was to analyze the plan quality metrics between the three techniques to assess the potential benefit of IMRT in an actual preclinical case. The treatment objective was to deliver a boost dose to a tumor subregion identified as being hypoxic. 3D-CRT has allowed this to be tested more precisely than typical cone deliveries and recent experiments using 3D-CRT in mouse models have been promising [13, 14]. More precise treatments in mice to the hypoxic region could provide stronger evidence of the need for oxygen-guided radiotherapy.

A murine CT volume with fibrosarcoma leg tumor had hypoxic regions ($pO_2 \leq 10$ torr) and normoxic regions (normal oxygen levels) determined by EPR (electron paramagnetic resonance) pO_2 imaging. The hypoxic region was .072cc and 21% of the total tumor vol-

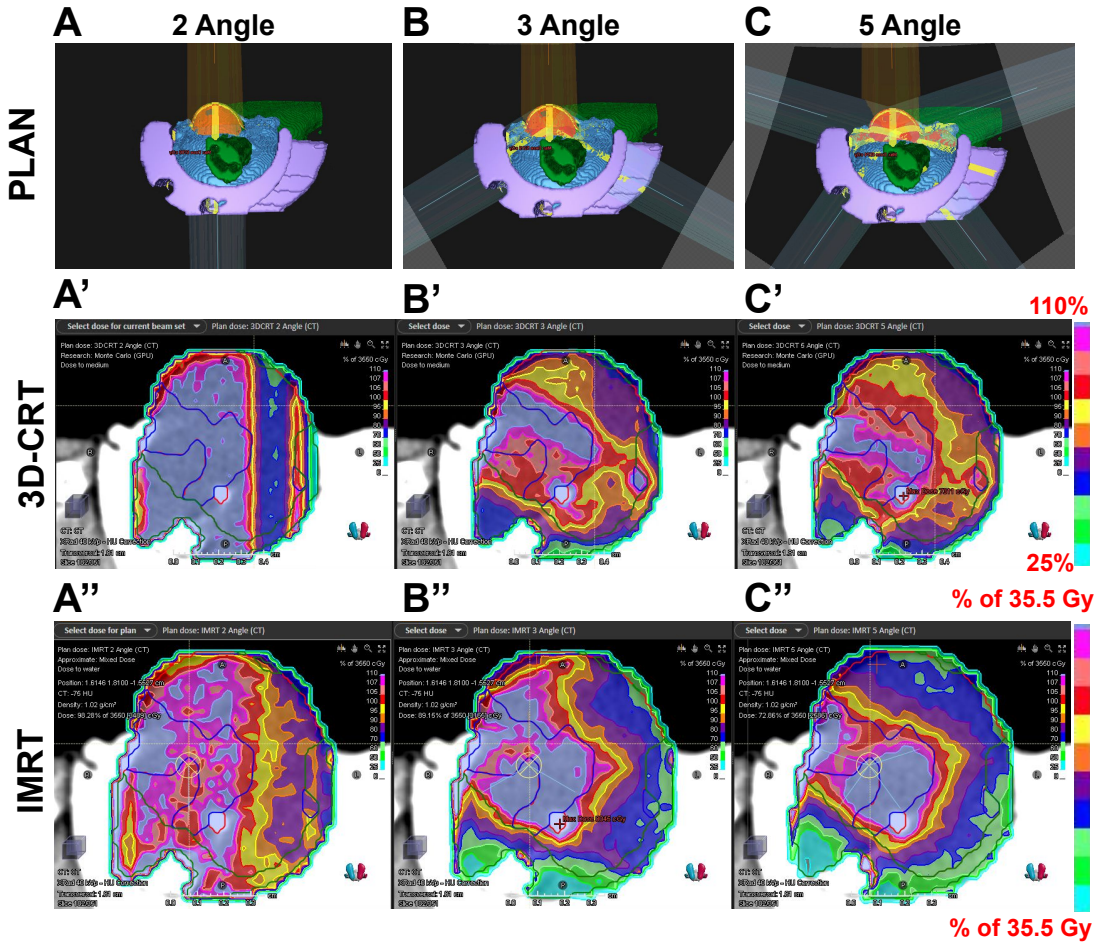

Figure 3.3: IMRT and 3D-CRT over 2, 3, and 5 Angles. A-C) illustrates the 3D visualization of the treatment plan with the tumor (red), healthy leg tissue (green), and polyvinyl siloxane cast for leg immobilization (cyan), and SLA resin bed (purple) segmented volumes shown, A'-C') show the dose distributions at isocenter for 3D-CRT with 2, 3, and 5 angles, A"-C") show the dose distributions at isocenter for IMRT with 2, 3, and 5 angles. Note all plans were normalized such that 95% of the hypoxic volume received 35.5 Gy and the dose color scale is the same between techniques and angles.

ume with 2 disconnected parts. The plan objective was to deliver a base 22.5 Gy to the entire tumor (PTV) and an extra 13 Gy to only the hypoxic target volume (HTV) while avoiding the normoxic target volume (NTV). Each plan was normalized so that 95% of the HTV received 35.5 Gy. IMRT and 3D-CRT plans with 2, 3, and 5 uniformly spaced angles were calculated. IMRT plans used an objective function to optimize fluence grid, while 3D-CRT

used a function to optimize conformal apertures based on segmentations in beam's eye view (BEV). Note the irradiator machine in μ-RayStation for the IMRT optimization was a template machine of the X-RAD 225Cx able to do fluence optimization for 1 mm bixels by using MLCs with 20 leaves of 2 mm width. This irradiator machine was provided by RaySearch Laboratories. For 3D-CRT, if multiple disjoint hypoxia contours were present in the BEV, then the disconnect segmentation tool was used to separate the hypoxic region into a contour for each disjoint hypoxic region. This was required for the automatic generation of conformal apertures.

For SAT, full arcs were done with the smallest possible cones given plan constraints. Plan metrics were calculated to assess plan quality. Paddick conformity index (CI) was the target volume in prescription isodose squared (22.5 or 35.5 Gy) divided by the total target volume times the total volume in prescription isodose. Dose spill around the hypoxic region (R83%) was the total volume in 29 Gy isodose (half-way between base and boost) divided by the total hypoxic volume.

Treatment Type		D95 [Gy]		Paddick CI [Gy]		
		NTV	HTV†	NTV	HTV	R83%
Cone	Parallel Opposed	23.3	35.5	.42	.14	7.4
	Static Arc	23.3	35.5	.48	.26	5.4
3D-CRT	2 Angle	23.6	35.5	.50	.29	3.9
	3 Angle	24.3	35.5	.56	.50	4.0
	5 Angle	24.3	35.5	.57	.49	4.1
IMRT	2 Angle	22.5	35.5	.50	.30	4.6
	3 Angle	22.4	35.5	.60	.52	3.3
	5 Angle	22.5	35.5	.63	.57	3.0

Table 3.1: Conformity and Dose Spill Across Treatment Types . The table illustrates dose metrics for conformity and dose spillage for a single murine case. Treatment objective was to deliver a base dose of 22.5 Gy to the entire tumor and boost dose of 13 Gy to the hypoxic. †Note all treatment types were normalized so that 95% of the hypoxic volume received 35.5 Gy (base + boost dose).

Based on the data, IMRT had the highest NTV and HTV conformity with the lowest dose spillage around boosted HTV compared to 3D-CRT and SAT. In the future, more segmented murine cases need to be imported into μ-RayStation. Further, it would be interesting to test how different parameters and characteristics such as gantry angle and tumor compactness influence the performance of treatment techniques. Additionally, optimization of beam weights for the 3D-CRT technique must be implemented for a fairer comparison to the IMRT approach. Lastly, the implementation of volumetric modulated arc therapy (VMAT), which is a radiotherapy technique that combines static arc with IMRT, would be interesting to model in μ-RayStation.

4

Conclusion

4.1 Summary of Work

The work demonstrates the applications of HPC-MC and GPU-MC for preclinical radiotherapy applications:

1. **Section 2.3**: A high-performance computing Monte Carlo Model (HPC-MC) for

the University of Chicago's X-RAD 225Cx small animal irradiator was developed and validated to film and ionization chamber measurements. The absolute mean dose difference between HPC-MC and film for the five commissioned collimators was 2% along the central beam axis in a water phantom. Beam attenuation measured with an ionization chamber found the half-value layer for Cu was 1.04 mm measured and 1.03 mm simulated. Additionally, a novel 3D-printed material copper polylactic acid (Cu-PLA), used in preclinical beam modulation, was modeled in HPC-MC with only 2% deviation to measurements.

2. **Subsection 2.4.1**: An empirical factor of 0.9 was determined to scale HPC-MC simulated dose calculations to real world irradiations. Scaling was normalized to the electronic charge used to generate the primary photon beam in the X-ray tube.

3. **Subsection 2.4.2**: An open-source pencil beam algorithm MatRad was validated to film measurements with a 3% absolute mean dose difference along the central beam axis in a water phantom. In the presence of 5 mm cortical bone insert at a depth of 1 cm in a tissue phantom, the absolute mean dose difference after the insert between HPC-MC and MatRad was 18% along the central beam axis, but only 2% in a homogeneous tissue phantom.

4. **Subsection 2.4.3**: An irradiation machine in μ-RayStation was commissioned using HPC-MC data with an absolute mean dose difference of 1% in the percent depth dose curve and 2% in the lateral beam profiles in a water phantom for the 2.4cm × 2.4cm reference field. The fast GPU Monte Carlo dose calculation approach of μ-RayStation was used as the GPU-MC in Chapter 3.

5. **Subsection 2.5.1**: Import of 3D-printed objects into HPC-MC for beam modulation was demonstrated with a photon fluence map after modulation and dose distribution at isocenter in a water phantom after delivery.

6. **Section 3.2**: GPU-MC retrospective treatment planning of oxygen-guided radiotherapy in five mice with SCC7 squamous carcinoma leg tumors with CBCT, MRI, and EPROI imaging was performed. Treatment plans used the 3D-conformal apertures, irradiation times, gantry angles, and bed shifts in the actual delivery.

7. **Section 3.3**: Parallel-opposed, static arc, 3D-conformal, and intensity-modulated radiotherapy were assessed in a murine CT volume with a fibrosarcoma leg tumor for oxygen-guided radiotherapy applications using GPU-MC.

4.2 Future Directions

Ultimately, HPU-MC and GPU-MC will help usher a much-needed paradigm shift in preclinical radiotherapy from dose to a patient to dose distributions within a patient. In other words, a more clinically analogous consideration of dose heterogeneities within preclinical models will be possible during preclinical radiotherapy experiments, especially through fast GPU-MC calculations. Some next steps are outlined below:

1. Beam modulation treatments like 3D-conformal and intensity-modulated radiotherapy in small animals should be validated in HPC-MC to film measurements.

2. The sub-cellular and cellular consequences of radiotherapy need to be studied using HPU-MC and TOPAS-nBio.

3. Integration of HPC-MC and GPU-MC through DICOM RT import and export will be vital for the validation of higher order preclinical treatment planning amd inverse planning optimization.

4. Results from GPU-MC retrospective treatment planning of a preclinical oxygen-guided radiotherapy experiment will need to be connected to survival outcomes.

5. Beam weighting in 3D-CRT GPU-MC of μ-RayStation will need to implemented along with a more rigorous investigation of inverse planning to optimize radiotherapy treatment plans.

6. Other preclinical radiotherapy experiments in different regions such as the brain, different irradiation setups like fully-shielded leg flank tumor models, and in general, more orthotopic/heterotopic tumor preclinical models will need to be studied using GPU-MC and HPC-MC.

In short, Monte Carlo will be vital for preclinical radiotherapy going forward.

References

[1] V. Valentini, L. Boldrini, S. Mariani, and M. Massaccesi. Role of radiation oncology in modern multidisciplinary cancer treatment. *Mol Oncol*, 14(7):1431–1441, Jul 2020.

[2] M. Baumann, N. Ebert, I. Kurth, C. Bacchus, and J. Overgaard. What will radiation oncology look like in 2050? A look at a changing professional landscape in Europe and beyond. *Mol Oncol*, 14(7):1577–1585, Jul 2020.

[3] R. L. Siegel, K. D. Miller, H. E. Fuchs, and A. Jemal. Cancer statistics, 2022. *CA Cancer J Clin*, 72(1):7–33, Jan 2022.

[4] R. L. Siegel, K. D. Miller, N. S. Wagle, and A. Jemal. Cancer statistics, 2023. *CA Cancer J Clin*, 73(1):17–48, Jan 2023.

[5] V. Dilalla, G. Chaput, T. Williams, and K. Sultanem. Radiotherapy side effects: integrating a survivorship clinical lens to better serve patients. *Curr Oncol*, 27(2):107–112, Apr 2020.

[6] W. Xiao, Y. Yuan, S. Wang, Z. Liao, P. Cai, B. Chen, R. Zhang, F. Wang, Z. Zeng, and Y. Gao. Neoadjuvant PD-1 Blockade Combined With Chemotherapy Followed by Concurrent Immunoradiotherapy in Locally Advanced Anal Canal Squamous Cell Carcinoma Patients: Antitumor Efficacy, Safety and Biomarker Analysis. *Front Immunol*, 12:798451, 2021.

[7] N. El-Sayes, A. Vito, and K. Mossman. Tumor Heterogeneity: A Great Barrier in the Age of Cancer Immunotherapy. *Cancers (Basel)*, 13(4), Feb 2021.

[8] Y. Zhuang, K. Liu, Q. He, X. Gu, C. Jiang, and J. Wu. Hypoxia signaling in cancer: Implications for therapeutic interventions. *MedComm (2020)*, 4(1):e203, Feb 2023.

[9] S. J. van Hoof, P. V. Granton, and F. Verhaegen. Development and validation of a treatment planning system for small animal radiotherapy: SmART-Plan. *Radiother Oncol*, 109(3):361–366, Dec 2013.

[10] L. Demetrius. Of mice and men. When it comes to studying ageing and the means to slow it down, mice are not just small humans. *EMBO Rep*, 6 Spec No(Suppl 1):39–44, Jul 2005.

[11] G. Redler, E. Pearson, X. Liu, I. Gertsenshteyn, B. Epel, C. Pelizzari, B. Aydogan, R. Weichselbaum, H. J. Halpern, and R. D. Wiersma. Small Animal IMRT Using 3D-Printed Compensators. *Int J Radiat Oncol Biol Phys*, 110(2):551–565, Jun 2021.

[12] P. S. Chen, W. T. Chiu, P. L. Hsu, S. C. Lin, I. C. Peng, C. Y. Wang, and S. J. Tsai. Pathophysiological implications of hypoxia in human diseases. *J Biomed Sci*, 27(1):63, May 2020.

[13] B. Epel, M. C. Maggio, E. D. Barth, R. C. Miller, C. A. Pelizzari, M. Krzykawska-Serda, S. V. Sundramoorthy, B. Aydogan, R. R. Weichselbaum, V. M. Tormyshev, and H. J. Halpern. Oxygen-Guided Radiation Therapy. *Int J Radiat Oncol Biol Phys*, 103(4):977–984, Mar 2019.

[14] I. Gertsenshteyn, B. Epel, M. Giurcanu, E. Barth, J. Lukens, K. Hall, J. F. Martinez, M. Grana, M. Maggio, R. C. Miller, S. V. Sundramoorthy, M. Krzykawska-Serda, E. Pearson, B. Aydogan, R. R. Weichselbaum, V. M. Tormyshev, M. Kotecha, and H. J. Halpern. Absolute oxygen-guided radiation therapy improves tumor control in three preclinical tumor models. *Front Med (Lausanne)*, 10:1269689, 2023.

[15] M. F. Gensheimer and Q. T. Le. Adaptive radiotherapy for head and neck cancer: Are we ready to put it into routine clinical practice? *Oral Oncol*, 86:19–24, Nov 2018.

[16] J. Patterson-Fortin and A. D. D'Andrea.) for Cancer Therapy. *Cancer Treat Res*, 186:285–298, 2023.

[17] S. J. Black, E. Kashkina, T. Kent, and R. T. Pomerantz. : A Unique Multifunctional End-Joining Machine. *Genes (Basel)*, 7(9), Sep 2016.

[18] G. S. Higgins, R. Prevo, Y. F. Lee, T. Helleday, R. J. Muschel, S. Taylor, M. Yoshimura, I. D. Hickson, E. J. Bernhard, and W. G. McKenna. A small interfering RNA screen of genes involved in DNA repair identifies tumor-specific radiosensitization by POLQ knockdown. *Cancer Res*, 70(7):2984–2993, Apr 2010.

[19] G. Rodriguez-Berriguete, M. Ranzani, R. Prevo, R. Puliyadi, N. Machado, H. R. Bolland, V. Millar, D. Ebner, M. Boursier, A. Cerutti, A. Cicconi, A. Galbiati, D. Grande, V. Grinkevich, J. B. Majithiya, D. Piscitello, E. Rajendra, M. L. Stockley, S. J. Boulton,

E. M. Hammond, R. A. Heald, G. C. M. Smith, H. M. R. Robinson, and G. S. Higgins. Inhibitors Provide Safe and Effective Tumor Radiosensitization in Preclinical Models. *Clin Cancer Res*, 29(8):1631–1642, Apr 2023.

[20] R. G. Syljuåsen. *Cell Cycle Effects in Radiation Oncology*, pages 1–8. Springer International Publishing, Cham, Oct 2019.

[21] F. Tillner, P. Thute, R. tof, M. Krause, and W. Enghardt. Pre-clinical research in small animals using radiotherapy technology–a bidirectional translational approach. *Z Med Phys*, 24(4):335–351, Dec 2014.

[22] L. A. Medina, B. I. Herrera-Penilla, M. A. Castro-Morales, P. pez, R. Jurado, E. rdenas, J. Chanona-Vilchis, and M. E. Brandan. Use of an orthovoltage X-ray treatment unit as a radiation research system in a small-animal cancer model. *J Exp Clin Cancer Res*, 27(1):57, Oct 2008.

[23] E. R. Biglin, G. J. Price, A. L. Chadwick, A. H. Aitkenhead, K. J. Williams, and K. J. Kirkby. Preclinical dosimetry: exploring the use of small animal phantoms. *Radiat Oncol*, 14(1):134, Jul 2019.

[24] J. Jeong, Q. Chen, R. Febo, J. Yang, H. Pham, J. P. Xiong, P. B. Zanzonico, J. O. Deasy, J. L. Humm, and G. S. Mageras. Adaptation, Commissioning, and Evaluation of a 3D Treatment Planning System for High-Resolution Small-Animal Irradiation. *Technol Cancer Res Treat*, 15(3):460–471, Jun 2016.

[25] S. Chiavassa, R. Nilsson, K. ment Colmou, V. Potiron, G. Delpon, and E. Traneus. -RayStation 8B. *Phys Med Biol*, 65(3):035006, Jan 2020.

[26] L. G. Marcu. Improving therapeutic ratio in head and neck cancer with adjuvant and cisplatin-based treatments. *Biomed Res Int*, 2013:817279, 2013.

[27] T. D. Chiu, T. J. Arai, J. Campbell Iii, S. B. Jiang, R. P. Mason, and S. Stojadinovic. MR-CBCT image-guided system for radiotherapy of orthotopic rat prostate tumors. *PLoS One*, 13(5):e0198065, 2018.

[28] C. S. Chui and S. V. Spirou. Inverse planning algorithms for external beam radiation therapy. *Med Dosim*, 26(2):189–197, 2001.

[29] K. R. Muralidhar, N. P. Murthy, A. K. Raju, and N. Sresty. Comparative study of convolution, superposition, and fast superposition algorithms in conventional radiotherapy, three-dimensional conformal radiotherapy, and intensity modulated radiotherapy techniques for various sites, done on CMS XIO planning system. *J Med Phys*, 34(1):12–22, Jan 2009.

[30] P. Alaei, B. J. Gerbi, and R. A. Geise. Evaluation of a model-based treatment planning system for dose computations in the kilovoltage energy range. *Med Phys*, 27(12):2821–2826, Dec 2000.

[31] N. Heidarloo, S. Mahmoud Reza Aghamiri, S. Saghamanesh, Z. Azma, and P. Alaei. A novel analytical method for computing dose from kilovoltage beams used in Image-Guided radiation therapy. *Phys Med*, 96:54–61, Apr 2022.

[32] C. Noblet, S. Chiavassa, F. Smekens, D. Sarrut, V. Passal, J. Suhard, A. Lisbona, F. Paris, and G. Delpon. Validation of fast Monte Carlo dose calculation in small animal radiotherapy with EBT3 radiochromic films. *Phys Med Biol*, 61(9):3521–3535, May 2016.

[33] A. Abdulle and J. C. L. Chow. Contrast Enhancement for Portal Imaging in Nanoparticle-Enhanced Radiotherapy: A Monte Carlo Phantom Evaluation Using Flattening-Filter-Free Photon Beams. *Nanomaterials (Basel)*, 9(7), Jun 2019.

[34] G. Saldana-Gonzalez, U. Reyes, H. Salazar, O. Martínez, E. Moreno, and R. Conde. High Density Devices Applied to a Gamma-Camera Implementation. In Dimitrios Ventzas, editor, *Advanced Image Acquisition, Processing Techniques and Applications*, chapter 2. IntechOpen, Rijeka, 2012.

[35] F. Verhaegen, S. van Hoof, P. V. Granton, and D. Trani. A review of treatment planning for precision image-guided photon beam pre-clinical animal radiation studies. *Z Med Phys*, 24(4):323–334, Dec 2014.

[36] C. Noblet, G. Delpon, S. Supiot, V. Potiron, F. Paris, and S. Chiavassa. A new tissue segmentation method to calculate 3D dose in small animal radiation therapy. *Radiat Oncol*, 13(1):32, Feb 2018.

[37] P. V. Granton and F. Verhaegen. On the use of an analytic source model for dose calculations in precision image-guided small animal radiotherapy. *Phys Med Biol*, 58(10):3377–3395, May 2013.

[38] A. Mesbahi and S. S. Zakariaee. Effect of anode angle on photon beam spectra and depth dose characteristics for X-RAD320 orthovoltage unit. *Rep Pract Oncol Radiother*, 18(3):148–152, 2013.

[39] D. S. Sharma, P. M. Dongre, V. Mhatre, and M. Heigrujam. Physical and dosimetric characteristic of high-definition multileaf collimator (HDMLC) for SRS and IMRT. *J Appl Clin Med Phys*, 12(3):3475, Apr 2011.

[40] S. Prajapati, B. Cox, P. Cadman, R. Jeraj, and T. Mackie. WE-E-108-07: Design of Open-Source Binary Micro MLC for Small Animal Radiotherapy: An OSMD Initiative. *Medical Physics*, 40(6):489–489, Jun 2013.

[41] Xu Z. The Size and Shape of a Single Photon. *Open Access Library Journal*, 8:1–22, 2021.

[42] J. Seco and F. Verhaegen. *Monte Carlo techniques in radiation therapy applications to dosimetry, imaging, and preclinical radiotherapy*. CRC Press, 2022.

[43] D.W. Kim, K. Park, H. Kim, and J. Kim. History of the Photon Beam Dose Calculation Algorithm in Radiation Treatment Planning System. *Prog Med Phys*, 31(3):54–62, Sep 2020.

[44] T. Zhuang, T. Djemil, P. Qi, A. Magnelli, K. Stephans, G. Videtic, and P. Xia. Dose calculation differences between Monte Carlo and pencil beam depend on the tumor locations and volumes for lung stereotactic body radiation therapy. *J Appl Clin Med Phys*, 14(2):4011, Mar 2013.

[45] N. Papanikolaou, J. J. Battista, A. L. Boyer, C. Kappas, E. E. Klein, T. R. Mackie, M. B. Sharpe, and J. Vandyk. Tissue Inhomogeneity Corrections for Megavoltage Photon Beams; AAPM Report No 85; Task Group No. 85; Task Group No. 65. *Medical Physics Publishing*, 85:1–135, 2004.

[46] B. A. Lulu and B. E. Bjärngard. A derivation of Batho's correction factor for heterogeneities. *Med Phys*, 9(6):907–909, 1982.

[47] M. B. Sharpe and J. J. Battista. Dose calculations using convolution and superposition principles: the orientation of dose spread kernels in divergent x-ray beams. *Med Phys*, 20(6):1685–1694, 1993.

[48] E. Tryggestad, M. Armour, I. Iordachita, F. Verhaegen, and J. W. Wong. A comprehensive system for dosimetric commissioning and Monte Carlo validation for the small animal radiation research platform. *Phys Med Biol*, 54(17):5341–5357, Sep 2009.

[49] R. Pidikiti. *Development of Monte Carlo Treatment Planning and Dosimetry System for Small Animal Irradiator*. PhD thesis, The University of Texas Southwestern Medical Center at Dallas, 2012.

[50] Z. Liu, C. Zheng, N. Zhao, Y. Huang, J. Chen, and Y. Yang. A GPU-accelerated Monte Carlo dose computation engine for small animal radiotherapy. *Med Phys*, 50(8):5238–5247, Aug 2023.

[51] M. Fisk, P. Rowshanfarzad, D. Pfefferlé, M. Fernandez de Viana, J. Cabrera, and M. A. Ebert. Development and optimisation of grid inserts for a preclinical radiotherapy system and corresponding Monte Carlo beam simulations. *Phys Med Biol*, 69(5), Feb 2024.

[52] R. Clarkson, P. E. Lindsay, S. Ansell, G. Wilson, S. Jelveh, R. P. Hill, and D. A. Jaffray. Characterization of image quality and image-guidance performance of a preclinical microirradiator. *Med Phys*, 38(2):845–856, Feb 2011.

[53] J. Allison, K. Amako, J. Apostolakis, P. Arce, M. Asai, T. Aso, E. Bagli, A. Bagulya, S. Banerjee, G. Barrand, B.R. Beck, A.G. Bogdanov, D. Brandt, J.M.C. Brown, H. Burkhardt, Ph. Canal, D. Cano-Ott, S. Chauvie, K. Cho, G.A.P. Cirrone, G. Cooperman, M.A. Cortés-Giraldo, G. Cosmo, G. Cuttone, G. Depaola, L. Desorgher, X. Dong, A. Dotti, V.D. Elvira, G. Folger, Z. Francis, A. Galoyan, L. Garnier, M. Gayer, K.L. Genser, V.M. Grichine, S. Guatelli, P. Guèye, P. Gumplinger, A.S. Howard, I. Hřivnáčová, S. Hwang, S. Incerti, A. Ivanchenko, V.N. Ivanchenko, F.W. Jones, S.Y. Jun, P. Kaitaniemi, N. Karakatsanis, M. Karamitros, M. Kelsey, A. Kimura, T. Koi, H. Kurashige, A. Lechner, S.B. Lee, F. Longo, M. Maire, D. Mancusi, A. Mantero, E. Mendoza, B. Morgan, K. Murakami, T. Nikitina, L. Pandola, P. Paprocki, J. Perl, I. Petrović, M.G. Pia, W. Pokorski, J.M. Quesada, M. Raine, M.A. Reis, A. Ribon, A. Ristić Fira, F. Romano, G. Russo, G. Santin, T. Sasaki, D. Sawkey, J.I. Shin, I.I. Strakovsky, A. Taborda, S. Tanaka, B. Tomé, T. Toshito, H.N. Tran, P.R. Truscott, L. Urban, V. Uzhinsky, J.M. Verbeke, M. Verderi, B.L. Wendt, H. Wenzel, D.H. Wright, D.M. Wright, T. Yamashita, J. Yarba, and H. Yoshida. Recent developments in Geant4. *Nuclear Instruments and Methods in Physics Research Section A: Accelerators, Spectrometers, Detectors and Associated Equipment*, 835:186–225, 2016.

[54] J. Allison, K. Amako, J. Apostolakis, H. Araujo, P. Arce Dubois, M. Asai, G. Barrand, R. Capra, S. Chauvie, R. Chytracek, G.A.P. Cirrone, G. Cooperman, G. Cosmo, G. Cuttone, G.G. Daquino, M. Donszelmann, M. Dressel, G. Folger, F. Foppiano, J. Generowicz, V. Grichine, S. Guatelli, P. Gumplinger, A. Heikkinen, I. Hrivnacova, A. Howard, S. Incerti, V. Ivanchenko, T. Johnson, F. Jones, T. Koi, R. Kokoulin, M. Kossov, H. Kurashige, V. Lara, S. Larsson, F. Lei, O. Link, F. Longo, M. Maire, A. Mantero, B. Mascialino, I. McLaren, P. Mendez Lorenzo, K. Minamimoto, K. Murakami, P. Nieminen, L. Pandola, S. Parlati, L. Peralta, J. Perl, A. Pfeiffer, M.G. Pia, A. Ribon, P. Rodrigues, G. Russo, S. Sadilov, G. Santin, T. Sasaki,

D. Smith, N. Starkov, S. Tanaka, E. Tcherniaev, B. Tome, A. Trindade, P. Truscott, L. Urban, M. Verderi, A. Walkden, J.P. Wellisch, D.C. Williams, D. Wright, and H. Yoshida. Geant4 developments and applications. *IEEE Transactions on Nuclear Science*, 53(1):270–278, 2006.

[55] S. Agostinelli, J. Allison, K. Amako, J. Apostolakis, H. Araujo, P. Arce, M. Asai, D. Axen, S. Banerjee, G. Barrand, F. Behner, L. Bellagamba, J. Boudreau, L. Broglia, A. Brunengo, H. Burkhardt, S. Chauvie, J. Chuma, R. Chytracek, G. Cooperman, G. Cosmo, P. Degtyarenko, A. Dell'Acqua, G. Depaola, D. Dietrich, R. Enami, A. Feliciello, C. Ferguson, H. Fesefeldt, G. Folger, F. Foppiano, A. Forti, S. Garelli, S. Giani, R. Giannitrapani, D. Gibin, J.J. Gómez Cadenas, I. González, G. Gracia Abril, G. Greeniaus, W. Greiner, V. Grichine, A. Grossheim, S. Guatelli, P. Gumplinger, R. Hamatsu, K. Hashimoto, H. Hasui, A. Heikkinen, A. Howard, V. Ivanchenko, A. Johnson, F.W. Jones, J. Kallenbach, N. Kanaya, M. Kawabata, Y. Kawabata, M. Kawaguti, S. Kelner, P. Kent, A. Kimura, T. Kodama, R. Kokoulin, M. Kossov, H. Kurashige, E. Lamanna, T. Lampén, V. Lara, V. Lefebure, F. Lei, M. Liendl, W. Lockman, F. Longo, S. Magni, M. Maire, E. Medernach, K. Minamimoto, P. Mora de Freitas, Y. Morita, K. Murakami, M. Nagamatu, R. Nartallo, P. Nieminen, T. Nishimura, K. Ohtsubo, M. Okamura, S. O'Neale, Y. Oohata, K. Paech, J. Perl, A. Pfeiffer, M.G. Pia, F. Ranjard, A. Rybin, S. Sadilov, E. Di Salvo, G. Santin, T. Sasaki, N. Savvas, Y. Sawada, S. Scherer, S. Sei, V. Sirotenko, D. Smith, N. Starkov, H. Stoecker, J. Sulkimo, M. Takahata, S. Tanaka, E. Tcherniaev, E. Safai Tehrani, M. Tropeano, P. Truscott, H. Uno, L. Urban, P. Urban, M. Verderi, A. Walkden, W. Wander, H. Weber, J.P. Wellisch, T. Wenaus, D.C. Williams, D. Wright, T. Yamada, H. Yoshida, and D. Zschiesche. Geant4—a simulation toolkit. *Nuclear Instruments and Methods in Physics Research Section A: Accelerators, Spectrometers, Detectors and Associated Equipment*, 506(3):250–303, 2003.

[56] J. Perl, J. Shin, J. Schumann, B. Faddegon, and H. Paganetti. TOPAS: an innovative proton Monte Carlo platform for research and clinical applications. *Med Phys*, 39(11):6818–6837, Nov 2012.

[57] B. Faddegon, J. ndez, J. Schuemann, A. McNamara, J. Shin, J. Perl, and H. Paganetti. The TOPAS tool for particle simulation, a Monte Carlo simulation tool for physics, biology and clinical research. *Phys Med*, 72:114–121, Apr 2020.

[58] Wikipedia. Cerrosafe — Wikipedia, the free encyclopedia. `https://en.wikipedia.org/wiki/Cerrosafe`, 2024. [Online; Accessed 5/2/2024].

[59] C. L. de Carvalho, A. F. Silveira, and D. d. o. s. S. Rosa. A study of the controlled degradation of polypropylene containing pro-oxidant agents. *Springerplus*, 2:623, 2013.

[60] M. Van der Walt, T. Crabtree, and C. Albantow. PLA as a suitable 3D printing thermoplastic for use in external beam radiotherapy. *Australas Phys Eng Sci Med*, 42(4):1165–1176, Dec 2019.

[61] H. P. Wieser, E. Cisternas, N. Wahl, S. Ulrich, A. Stadler, H. Mescher, L. R. ller, T. Klinge, H. Gabrys, L. Burigo, A. Mairani, S. Ecker, B. Ackermann, M. Ellerbrock, K. Parodi, O. kel, and M. Bangert. Development of the open-source dose calculation and optimization toolkit matRad. *Med Phys*, 44(6):2556–2568, Jun 2017.

[62] National Institute of Standards and Technology. X-Ray Mass Attenuation Coefficients. `https://physics.nist.gov/PhysRefData/XrayMassCoef/tab2.html`, 2024. [Online; Accessed 5/2/2024].

[63] M. Toulany. Targeting DNA Double-Strand Break Repair Pathways to Improve Radiotherapy Response. *Genes (Basel)*, 10(1), Jan 2019.

[64] J. Schuemann, A. L. McNamara, J. ndez, J. Perl, K. D. Held, H. Paganetti, S. Incerti, and B. Faddegon. TOPAS-nBio: An Extension to the TOPAS Simulation Toolkit for Cellular and Sub-cellular Radiobiology. *Radiat Res*, 191(2):125–138, Feb 2019.

[65] K. Jabbari. Review of fast monte carlo codes for dose calculation in radiation therapy treatment planning. *J Med Signals Sens*, 1(1):73–86, Jan 2011.

[66] D. Terribilini, M. K. Fix, D. Frei, W. Volken, and P. Manser. VMC++ validation for photon beams in the energy range of 20-1000 keV. *Med Phys*, 37(10):5218–5227, Oct 2010.

[67] C. Pinter, A. Lasso, A. Wang, D. Jaffray, and G. Fichtinger. SlicerRT: radiation therapy research toolkit for 3D Slicer. *Med Phys*, 39(10):6332–6338, Oct 2012.

Other Acknowledgements:

During college, I have been fortunate to be funded by the Biological Sciences Collegiate Division (BSCD) and College Center for Research and Fellowships (CCRF) at the University of Chicago. In particular, I would like to thank these programs: BSCD Summer Undergraduate Research Fellowship in Bioimaging for Oncology and Related Disciplines (SURFBOARD) for two summers, CCRF QUAD Summer Undergraduate Research Grant for a summer, and CCRF QUAD Academic Year Undergraduate Research Grant for four academic quarters.

Partially funding for this work was provided by the NIH S10-OD025081, S10-RR021039, and P30-CA14599 awards. The contents of this thesis are solely the responsibility of the author and do not necessarily represent the official views of any of the supporting organizations.

This thesis was typset using LaTeX, originally developed by Leslie Lamport and based on Donald Knuth's TeX. The body text is set in 11 point Egenolff-Berner Garamond, a revival of Claude Garamont's humanist typeface. A template that can be used to format a PhD thesis with this look and feel has been released under the permissive MIT (X11) license, and can be found online at github.com/suchow/Dissertate or from its author, Jordan Suchow, at suchow@post.harvard.edu.

Sources with a PubMed ID were cited using the "TeXMed - a BibTeX interface for PubMed" tool which can be found online at https://www.bioinformatics.org/texmed/ and was written by Arne Muller.